Cyclic anoxia and organic rich carbonate sediments within a drowned carbonate platform linked to Antarctic ice volume changes: Late Oligocene-early Miocene Maldives

Cyclic Anoxia and Organic Rich Carbonate Sediments within a Drowned Carbonate Platform linked to Antarctic ice volume changes: Late Oligocene-Early Miocene Maldives

P. K. Swart[1], C. L. Blättler[2], M. Nakakuni[3], G.J. Mackenzie[1], C. Betzler[4], G. P. Eberli[1], J. Reolid[4], M. Alonso-García[5], A. L. Slagle[6], J. D. Wright[7], D. Kroon[8], J.J.G. Reijmer[9], A. L. Hui Mee[1] J. R. Young[10], C.A. Alvarez-Zarikian[11], O. M. Bialik[12], J. A. Guo[13], S. Haffen[14], S. Horozal[15], M. Inoue[16], L. Jovane[17], L. Lanci[18], J. C. Laya[19], T. Lüdmann[4], B. N. Nath[20], K. Niino[21], L. M. Petruny[22], S. D. Pratiwi[23], X. Su[24], C.R. Sloss[25], Z. Yao[26,27]

[1]Department of Marine Geosciences, RSMAS, University of Miami, Miami FL 33149, USA.
[2]Department of the Geophysical Sciences, University of Chicago, Chicago IL 60637, USA.
[3]Department of Environmental Engineering for Symbiosis, Soka University, 1-236 Tangi-cyo, Hachioji-shi Tokyo 192-0003, Japan.
[4]Institute of Geology, CEN, University of Hamburg, Bundesstrasse 55, Hamburg 20146, Germany.
[5]Instituto Portugues do Mar e da Atmosfera (IPMA), Divisão de Geologia e Georecursos Marinhos, Rua Alfredo Magalhães Ramalho, 6, 1495-006 Lisboa, Portugal: Centro de Ciencias do Mar (CCMAR), Universidade do Algarve, Faro, Portugal.
[6]Lamont-Doherty Earth Observatory, Columbia University, Borehole Bldg. 61 Route 9W, Palisades NY 10964, USA.
[7]Department of Geological Sciences, Rutgers, The State University of New Jersey, 610 Taylor Road, Piscataway NJ 08854-8066, USA.
[8]School of GeoSciences, University of Edinburgh, Grant Institute, The King's Buildings, West Mains Road, Edinburgh EH9 3JW, UK.
[9]Department of Earth and Life Sciences, Vrije Universiteit Amsterdam, De Boelelaan 1085, HV Amsterdam, The Netherlands.
[10]Department of Earth Sciences, University College London, Gower Street, London WC1E 6BT, UK.
[11]International Ocean Discovery Program, Texas A&M University, Discovery Drive, College Station TX 77845, USA.
[12]Dr. Moses Strauss Department of Marine Geosciences, The Leon H. Charney School of Marine Sciences, University of Haifa, Carmel 31905, Israel.
[13]Department of Geological Sciences, California State University Bakersfield, 9001 Stockdale Highway, Bakersfield, CA 93311, USA.
[14] GeoRessources lab., UMR 7359, Ecole Nationale Supérieure de Géologie, Université de Lorraine, CNRS, CREGU, 2 Rue du Doyen Marcel Roubault,Vandoeuvre-lès-Nancy, F-54501, France
[15]Petroleum and Marine Research Division, Korea Institute of Geoscience & Mineral Resources (KIGAM), Gwahang-no 124, Yuseong-gu, Daejeon 305-350, Korea.
[16]Graduate School of Natural Science and Technology, Okayama University, 3-1-1 Tsushima-naka 700-8530, Japan.
[17]Instituto Oceanográfico da Universidade de São Paulo, Praça do Oceanográfico, 191, São Paulo, SP 05508-120, Brazil.8
[18]Istituto di Scienze della Terra, Università di Urbino, Via S. Chiara 27, Urbino 61029, Italy.
[19]Department of Geology and Geophysics, Texas A&M University, Mail Stop 3115, College Station TX 77843-3115, USA.
[20]Geological Oceanography Division, CSIR-National Institute of Oceanography, Dona Paula Goa 403004, India.
[21]Graduate School of Science and Engineering, Yamagata University, 1-4-12 Kojirakawa-machi, Yamagata City 990-8560, Japan.
[22]Earth and Environmental Sciences, University of Technology Queensland, R-Block 317, 2 George Street, Brisbane Queensland 4001, Australia.
[23]Department of Geological Engineering, Faculty of Earth Technology and Energy, Universitas Trisakti, Jakarta-Indonesia.
[24] Key Laboratory of Marginal Sea Geology, South China Sea Institute of Oceanology, Chinese Academy of Sciences, West Xingang Road, Guangzhou 510301, P.R. China.
[25]Earth and Environmental Sciences, University of Technology Queensland, R-Block 317, 2 George Street, Brisbane Queensland 4001, Australia.
[26] Department of Marine Geology, First Institute of Oceanography (FIO) State Oceanic Administration (SOA), #6 Xian Xia Ling Road, Qingdao Shandong Province 266061, P.R. China.
[27]Laboratory for Marine Geology, Qingdao National Laboratory for Marine Science and Technology, Qingdao, P.R. China.

ABSTRACT

This paper reports the newly discovered occurrence of thick sequences (~ 100 m) of Late Oligocene-Early Miocene interbedded organic carbon-rich sediments (sapropels) and pelagic (organic carbon poor) carbonates (~24.5 to 21.5 Ma) at Sites U1466 and U1468 drilled in the Maldives archipelago during the ~~Integrated Ocean Discovery~~ Expedition (~~IODP~~) 359. This occurrence is unusual in that it is located > 1000 m above the surrounding ocean floor within an inter-atoll basin and not linked to any known global oceanic events. Total organic carbon content reached as high as 35 % in the darker layers, while the interbedded carbonates have concentrations of less than 0.1%. Trace elements characteristic of anoxic waters, such as Mo, V, Cr, U, and Pb, correlate positively with concentrations of organic carbon. Nitrogen isotopic data show no evidence that the intervals of high total organic carbon are related to enhanced productivity driven by upwelling. Instead, high organic carbon is associated with intervals of anoxia. We propose that sea level fluctuations linked to Antarctic ice volume changes restricted exchange with the open ocean causing bottom waters of the inter-atoll basin to become anoxic periodically. The architecture of the platform at the end of the Oligocene combined with the global sea level highstand set the stage for orbitally-driven sea level changes producing cyclic deposition of sapropels. The proposed mechanism may serve as an analogue for other occurrences of organic carbon-rich sediments within carbonate platform settings.

1. INTRODUCTION

Organic-rich deposits are abundant in the geological record (Algeo, 2004; Arthur, 1979; Jenkyns, 2010; Parrish and Curtis, 1982; Sageman et al., 2003; Schlanger and Jenkyns, 1976). Whilst many ancient examples are thought to be related to global anoxic events, there are few examples associated with the development of carbonate platforms (Gardner et al., 2013; Koster et al., 1988) and isolated basins (Emeis and Weissert, 2009; Lyons, 1991; Peterson et al., 1991), where restricted ventilation or enhanced productivity caused the preservation of TOC. Here, we report on the newly discovered occurrence of a sequence of alternating organic-rich and -poor sediments from ~~Integrated~~ Ocean Discovery ~~Project~~ (IODP) Sites U1466 and U1468 in the Maldives Inner Sea (Indian Ocean), examining the possible conditions that led to the formation of this unusual deposit in an inner-atoll basin through geochemical and associated with orbitally-driven Antarctic ice volume changes, and suggest that the inter-atoll environment of the Maldives may serve as an analogue system for other known organic-rich deposits with previously unclear origins.

1.1 Background

This study deals with samples from two ~~cores~~ from the Maldives recovered during Expedition 359 of the ~~Integrated~~ Ocean Discovery ~~Project~~ (IODP) (Betzler et al., 2016a). These sediments are comprised of a ~3 km thick shallow water and hemipelagic carbonate succession (Aubert and Droxler, 1992) that formed on a lower Paleogene (60–50 Ma) volcanic basement (Duncan and Hargraves, 1990). Although the primary aim of drilling during IODP Expedition 359 was to examine timing of the commencement of the

South Asian Monsoon (Betzler et al., 2018; Betzler et al., 2016b), drilling also revealed, a ~100 m section of interbedded hemi-pelagic sediments rich in organic carbon at Sites, U1466 and U1468 (Fig.1), similar to those found in ocean-wide anoxic events.

2. METHODS

Samples were taken from every dark layer and intervening light colored layers between ~ 700 and 800 mbsf at Site U1466 and between ~720 and 805 mbsf at U1468. High-resolution sampling was conducted in two core sections, U1466B-56R-1W and U1468A-105X-1W, where 2 cm^3 samples were taken at ~ 2 cm intervals (Fig. 2).

2.1 Organic $\delta^{13}C$ and $\delta^{15}N$ values and Acid-insoluble material

Co-occurring sedimentary organic material was isolated via dissolution in 5 % HCl acid following the method described in Oehlert et al. (2012). The organic carbon residual was combusted in a Costech ECS 4010 (Costech Analytical Technologies, Inc.) Water was removed and oxygenated species of nitrogen reduced to N_2 using a Cu furnace held at 600°C in the standard manner. For C and N isotopic measurements, the CO_2 and N_2 gases produced were transferred to a continuous flow stable isotope ratio mass spectrometer (Thermo Delta V Advantage). The $\delta^{13}C$ and $\delta^{15}N$ values of the samples are reported relative to the V-PDB (Vienna Pee Dee Belemnite) scale and atmospheric nitrogen respectively. The V-PDB scale for organic carbon is defined by the $\delta^{13}C$ value of graphite (USGS24) = -16.05‰ versus V-PDB (Coplen et al., 2006). Within each run (typically 50 samples), a glycine and secondary standard were analyzed every ten samples. The reproducibility of $\delta^{13}C$ and $\delta^{15}N$ values of the standards was ±0.1 and ±0.3

‰ respectively.

2.2 Insoluble Residue and Total Organic Carbon

Weights and percentages of insoluble residue and total organic matter (TOC) were analyzed and calculated following the methods of Oehlert et al. (2012). The standard deviation of these analyses is 0.4 wt% based upon repeated analyses of glycine (n=54).

2.3 Inductively Coupled Plasma Mass Spectrometry (ICP-MS)

Samples from Core Section U1466-56X-1 were analyzed for a range of major and trace elements (Li, Na, Mg, Al, K, Ca, Ti, V, Cr, Mn, Fe, Sr, No, Cd, Pb, Th, and U) using a quadrupole ICP-MS (Thermo iCAP-Q) at Princeton University. The method thoroughly dissolved the carbonate phase and partially dissolved other mineral phases and organic matter so the values analyzed represent a maximum value for the carbonate phase and a minimum of the bulk sample. Approximately 10 to 25 mg samples of bulk sediment were weighed out directly into clean, acid-washed Teflon beakers. The samples were dissolved by adding 5 mL of concentrated (~16 N) distilled nitric acid, capping the beakers, and heating them at ca. 75 °C for over 12 hours. The beakers were then opened and dried down, and an additional 2 mL of concentrated nitric acid was added and dried down. The samples were then redissolved in 5 mL of 2% nitric acid. All mineral components appeared to be dissolved, although some brown detritus resembling remnant organic matter sometimes remained. After centrifugation, the clear supernatant was diluted up to 200x to yield solutions of approximately 10 ppm Ca. Trace element analyses were performed with matrix-matched standards at approximately 10 ppm Ca and with

varying trace element concentrations to bracket those in the samples. Internal errors are better than 3% (RSD).

2.4 X-Ray Fluorescence

The XRF scans were measured at the Ocean Drilling and Sustainable Earth Science (ODASES) XRF scanning facility at the IODP Gulf Coast Repository (GCR) in College Station, Texas (USA) using a third generation AvaaTech XRF scanner configured to analyze split sediment core halves for elements between Mg and U in the periodic table (Lyle and Backman 2013). The data were acquired with a Canberra X-PIPS Silicon Drift Detector (SDD) with 150 eV X-ray resolution at 5.9 keV and a Canberra Digital Spectrum Analyzer model DAS 1000. The X-Ray source was an Oxford Instruments 100 W Neptune X-ray tube with a rhodium (Rh) target. Raw spectral data were processed using the Canberra WINAXIL software package to produce elemental intensity data. The dual slit system was set to provide down-core spatial resolution of 10 mm and cross-core spatial resolution of 12 mm. The system was set to perform two consecutive runs of the same section, the first one at 9 kV, 0.25 m A and 6 s, and the second one at 30kV, 1.25 mA and 6 s. The first scan provides data for the elements Mg, Al, Ba, Ca, Cl, Cr, Fe, K, Mn, P, S, SI, Rh, and Ti, and the second for Bi, Cd, Cu, Br, Fe, Ga Nb, Ni, Mo, Pb, Rb, Sr, Y, Zn, and Zr. Each core section was removed from refrigeration at least 2 hours before scanning and scraped to clean and smooth the core surface. The split core surface was covered with 4 μm thick Ultralene plastic film to prevent contamination of the X-ray detector. Measurements were taken at 3 cm intervals whenever possible. Because measurements cannot be performed if the sediment presents cracks or uneven surface some measurements were skipped or shifted to the nearest suitable area. In addition,

Core Sections U1466B-56R-1W and 2W were analyzed at 1 cm resolution. In order to evaluate the reliability of the analysis of certain elements (Fe, Al, Sr, Si K, Ca, Br, Mo, and Ba) a companion study (Kunkelova et al., 2018) analyzed samples of pressed pellets using a fully quantitative conventional XRF method. That study measured 67 samples from Cores 359-U1467C-4H to -6H on a conventional XRF instrument in Edinburgh with the same pellets measured on the AvaaTech XRF core scanner College Station ~~in~~ Texas. For these 1 g aliquots of core material were ground in an agate mortar and pestle and then pressed into 1 cm diameter pellets using a pellet press operating at a pressure of 2 t/cm2. Pellets were analyzed on a Philips PW2404 XRF spectrometer with a Rh-anode X-ray tube. Corrections for matrix effects on the intensities for major element lines were made using theoretical alpha coefficients calculated using Philips software (Reynolds, 1963). Intensities of the longer-wavelength trace element lines were corrected for matrix effects using alpha coefficients based on major element concentrations. For other trace elements, matrix corrections were applied using the Rh K alpha Compton scatter line as an internal standard. Line overlap corrections were applied using synthetic standards. The spectrometer was calibrated with 15 USGS and CRPG standards using the values given in (Govindaraju, 1994).

2.5 Inorganic Stable Carbon and Oxygen Isotopes

Carbonate materials were reacted with phosphoric acid using a common acid bath at 90°C and the CO_2 released analyzed using a dual-inlet mass spectrometer (Finnigan-MAT 251 at the University of Miami. The CO_2 gas was calibrated using NBS-19 (National Bureau of Standards) and reported relative to V-PDB using the conventional notation.

Replicate analyses yielded a precision < 0.1‰ for both $\delta^{13}C$ and $\delta^{18}O$ values.

2.6 Fatty acids

In intervals with high organic content, sediment samples from Hole U1466B were obtained to analyze fatty acids. Fatty acids were analyzed using an on-line TMAH (tetramethylammonium hydroxide) thermochemolysis. Finely powdered and dried sediment sample (ca. 14 mg) was placed in a pyrofoil (foil for pyrolysis) and TMAH reagent (97%, Sigma-Aldrich Co., 25 wt.% methanol; 40 µL) was added. After methanol was evaporated to dryness, the pyrofoil was wrapped and set into a Curie point pyrolyzer (JHP-3: Japan Analytical Industry Co.) and heated at 315°C for 20 s. The resulting TMAH products were introduced into a GC column (DB-5ms, 30m x 0.32mm i.d.; 0.25µm film thickness) and analyzed by MS (5975C; Agilent Technologies Co.).

2.7 Downhole Logging

Total and spectral natural gamma radiation (NGR) was measured at 30-cm resolution with a 15-cm sampling interval using standard shipboard methods employed by IODP as described by Betzler et al. (2017).

2.8 Statistical Methods

Factor analysis was performed using Statistica 8.0 and spectral analysis using MATLAB™ (https://www.mathworks .com). Ages were calculated using the shipboard biostratigraphy (Betzler et al., 2017) and the data were interpolated using a linear method to an interval of 10,000 years (Davis, 1973). Spectral analyses were performed using

Tukey weights and smoothing window of five points. Factor analysis was performed on the ICP-MS data and the results normalized using a Varimax method.

2.9 Scanning Electron Microscopy

Selected samples were examined from Core U1446B-56R in both the dark and light layers. Small rock chips were mounted on aluminum stubs using epoxy resin, sputter coated with gold-palladium and examined using a Zeiss Ultra Plus Field Emission SEM at the British Natural History Museum.

3. RESULTS

3.1 Age Model

The ages of the sediments were determined by micropaleontologists on the drilling expedition. The integrated nannofossil and planktonic foraminiferal stratigraphy provides a robust biostratigraphic framework for this carbonate sequence representing drowning of an ancient shallow water carbonate platform. Several reliable biostratigraphic events were placed with a high degree of certainty. These include the first occurrence of *Paragloborotalia kugleri*, which indicates the Oligocene/Miocene boundary, and the last occurrence of the late Oligocene species *Sphenolithus ciperoensis*. The description of the sedimentology, age, and various chemical and physical properties can be found in the initial scientific reports (Betzler et al., 2016b) and additional publications (Betzler et al., 2016a; Betzler et al., 2018).

228

229 **3.2 Sedimentology**

230 The intervals containing the dark-light cycles (715.34-803.61 mbsf in Site U1466 and
231 728.6-817.55 mbsf in Site U1468) overlie an Oligocene carbonate platform and a
232 succession of shallow-water deposits (Betzler et al., 2016b) (Fig. 1B). These sediments
233 consist of wackestone, locally and gradually changing into mudstone or packstone and
234 display an alternation of laminated and poorly bioturbated dark intervals with highly to
235 completely bioturbated light intervals (Fig. 3). Sediments in the dark intervals have
236 abundant planktonic foraminifers, fish debris and nannofossils suggesting open marine
237 conditions. The dark layers are finely laminated and locally show scattered discrete small-
238 sized burrows of *Thalassinoides*, *Phycosiphon*, *Palaeophycus*, and *Planolites*. The dark
239 intervals range in thickness from 1 to 25 cm and are intercalated with light wackestone
240 intervals of 5 to 300 cm thick. The sediments in the light intervals are highly bioturbated
241 and are comprised of abundant planktonic foraminifers and nannofossils (Fig. 4). Fish
242 debris are rare to barren.

243

244 **3.3 Organic Content**

245 The darkness of the sediments is related to the TOC of the sediment, which varies
246 between <0.1% within the light layers to as high as 35 % in one of the dark layers. The
247 mean TOC (± 1σ) for the dark layers is 8.78±5.6% and 5.77±6.4 % for Sites U1466 and
248 U1468, respectively, compared to the light layers which have TOC of 0.73 ± 0.78% and
249 0.15 ±0.22%. In both Sites 1466 and 1468, the intervals with the highest TOC, are found
250 towards the base on the dark and light interval (Fig. 5 & 6).

3.3.1 Carbon and Nitrogen Isotopic Composition

The mean $\delta^{13}C$ values of the TOC ($\delta^{13}C_{TOC}$) are –20.9 ‰ at Site U1466 and -22.7 ‰ at Site U1468; there was no statistically significant (SS) variation between the dark and light layers. However, there is a gradual increase in the $\delta^{13}C$ values from the base of both Sites U1466 and U1468 to approximately the top of the interval in which the dark and light layers are found. In Site U1466, the increase in $\delta^{13}C$ values is from -23 to -17 ‰ while at Site U1468 the $\delta^{13}C$ value increases from -24 to -20 ‰. Within the zone of dark and light alternations, the $\delta^{15}N$ values of the TOC range from -1 to +2 ‰ with the organic-rich zones generally expressing more negative $\delta^{15}N$ values (Fig. 8).

3.3.2 Fatty Acids

Most of the fatty acids are in the range from C_{12} to C_{32}, with dominance of C_{14}–C_{18} fatty acids (supplemental material, S1). There is a statistically significant increase in C_{24}–C_{32} fatty acids below ~770 mbsf and the ratio of C_{24}–C_{32} fatty acids to C_{14}–C_{18} fatty acids (long/short ratio) increases towards the base of the dark and light interval.

3.3.3 CN Ratio

The C/N ratio of the organic material varied between 10 and 20 with no statistically significant differences between the dark and light layers. Site U1468 has higher C/N ratios than U1466 ($p<0.05$), and the CN ratio increases towards the bottom of the section.

3.4 Carbonate

3.4.1. Oxygen and Carbon Isotopic Composition

Within Core U1466B-56R there is an alternation of ~1‰, in the $\delta^{18}O$ values, the increase of which leads the increase in TOC (Fig. 7). The amplitude of these cycles is similar to the early Miocene benthic cycles of $\delta^{18}O$ values in foraminifera noted during the same time on Ceara Rise (Zachos et al. 2001). Similar associations were noted in Core U1468A-105X. However, overall the $\delta^{18}O$ values of the dark layers (-1.86 ‰ in Site U1466 and -2.29‰ in Site U1468) are slightly more negative than the light layers (-1.60‰ in Site U1466 and -1.96‰ in Site U1468). The $\delta^{13}C$ values of the carbonate components are more negative within the dark layers compared to the light layers (+0.84‰ vs. +1.28 ‰ in Site U1468; +0.97‰ vs +1.24‰ in Site U1466 (p<0.01)) (Fig. 7).

3.4.2. Trace Elemental Analysis

X-ray Fluorescence Scanning

The following elements (Ba, Br, Cd, Fe, Cu, Mo, Pb, S, Y, and Zn) showed a strong positive correlation between each other and with the concentration of TOC in the cores (Fig. 8 and 9). Generally, there is a sharp rise in concentration of trace elements at the bottom of each dark interval mirroring changes in the ‘darkness’ of these intervals.

Wet Chemical Analyses

293 Samples from Section U1466B-56R-1 were analyzed for a range of elements using
294 Inductively Coupled Plasma- Mass Spectrometry (ICP-MS). Whilst some of the elements
295 analyzed were the same as those measured using XRF (Ca, Fe, Mo, Pb, and Sr), several
296 others (Cr, Th, U, and V) were only analyzed using ICP-MS and provide important
297 additional information on the redox state and origin of the sediments. The concentration
298 of certain elements (Ca, Fe, Mo, Pb, Al, and Sr) measured using ICP-MS are generally
299 correlated with intensities measured using XRF, albeit with a lag of ~ 2-4 cm (See
300 supplemental material, S2 for cross plots between XRF and ICP-MS data and
301 discussion). For other elements (Cr, Ba, and Mg) no correlation was observed between
302 the two methods (See supplemental material. Analogous to the XRF data, the
303 concentration of a number of elements (Al, Ba, Cd, Cr, Fe, Li, Mo, Pb, Th, V, and U) were
304 positively correlated with TOC in this core (Fig. 7). Principal component analysis shows a
305 preferential clustering of Al, Cd, Cr, Fe, K, Li, Mo, Pb, Th, U, and V accounting for 54%
306 of the variance (supplemental material, Fig. S3-11).

307 *Comparison to Quantitative XRF Analyses*

308 Correlation coefficients range from about < 0.1 to ~0.9 with K and Si having the highest
309 values of about 0.9. Elements such as Fe, SI, and Al showed a R^2 values > 0.8. A full
310 comparison of the results from both methods are included in the supplemental material
311 (S1).

312

313 *3.4.3. Natural Gamma*

314 At all sites, spectral natural gamma ray (NGR) logs show that the NGR signal is almost
315 entirely the result of variations in the concentration of U, with K and Th contributing only
316 a minor proportion of the total signal (Betzler et al., 2017). The NGR signal routinely
317 shows a positive correlation with the concentration of TOC (R^2=0.40, n=88 for Site U1468)
318 and R^2=0.36, n=71 for Site U1466) and can be used to correlate core material with
319 downhole logging data, which include in situ total and spectral NGR. Based on changes
320 in the downhole NGR signal, between 30 and 35 dark layers were identified between 24.5
321 and 21.5 Ma, only some of which were recovered during drilling. A spectral analysis of
322 these data show peaks at ~ 100 and 50 K years (Fig. 10a).

323 *3.4.4. Resistivity*

324 The resistivity signal obtained from downhole logging was strongly correlated with the
325 Gamma ray signal. As this tool was located lower on the logging string than the Gamma
326 tool a further 22 m of section could be logged in Hole U1468. A spectral analysis of these
327 data (Fig. 10b) show peaks around 120, 80, and 40K years.

328

329 ## 4. DISCUSSION

330 Previous work has shown that a rimmed platform with a protected basin developed in the
331 Maldives during the Early to Late Oligocene transition when shallow-water carbonate
332 production became restricted to narrow bands at the ocean-ward edges, forming a saucer
333 shape basin perhaps 50-100 m deep (Betzler et al., 2018). The platform drowning at the
334 Oligocene-Miocene transition coincided with a major sea level rise during the early
335 Miocene with an amplitude of approximately 50 m (Miller et al., 2011) and is perhaps

synchronous with platform drowning events recognized in other locations (Mutti et al., 1997). The drowning in the Maldives is coincident with the development of the sapropels described in this paper.

4.1. Nature of the Dark and Light Layers

While many factors can contribute to the origin of color differences including variations in trace elements such as Fe, it is likely that the major cause of variations in these cores arise from variations in the amount of organic material within the darker layers, identified simply on a subjective inspection of color, containing an average of between 5.8 and 9.8 wt % compared to the lighter colored intervals (0.16 to 0.73 wt %). Whilst the presence of abundant oceanic biota suggests that oceanic conditions were prevalent during deposition of both dark and light layers, the darker ones have the characteristics of sediments deposited in anoxic basins including a high TOC (2-39 %) and an abundance of redox-sensitive trace elements (Brumsack, 2006; Tribovillard et al., 2006). In contrast to the light layers, the darker intervals have smaller burrows and low bioturbation indices, also clear indicators of reduced oxygenation or enhanced productivity (Reolid and Betzler, 2018).

The occurrence of such layers is normally thought to be result from either enhanced productivity or through the enhanced preservation of organic material. Reduced organic concentration as a result of sediment dilution which has been proposed in some instances (Bohacs, 2005) to account for variations in the amount of organic material. However, this is not considered to be a realistic option in this case. In reality, most such occurrences arise from a combination of both productivity and preservation, although additional geochemical patterns can indicate the relative importance of these two effects.

359

360 *4.2. Productivity*

361 An enhanced productivity origin of the high TOC within the darker layers is supported by
362 slightly higher concentrations of nutrient-related elements such as Cd and to a lesser
363 extent Ba, Cu, and Zn. While the interpretation of variations in these elements is not
364 straight forward (Tribovillard et al., 2006), in some instances higher concentrations of
365 these elements are related to upwelling and hence higher inputs of nutrients such as
366 nitrate and phosphate (Boyle, 1981; Lea and Boyle, 1991). Such upwelling might occur
367 along the margins of the platform, influencing productivity within the water over the
368 platform. However, upwelled waters should have been influenced by denitrification and
369 hence the organic components should have had relatively positive $\delta^{15}N$ values (Altabet
370 and Deuser, 1985). This is contrary to is observed with the organic matter in the dark
371 layers having $\delta^{15}N$ values close to 0‰ (Fig. 7). This suggests that nitrogen fixation, rather
372 than upwelled nitrate, was the major source of nitrogen for the organic production.
373 Another potential source of nutrients in the darker layers, is atmospheric dust (Figs. 7 -
374 9). These layers are elevated in Al, K, Li, and Fe. Considering that the Maldives are not
375 significantly influence by riverine source it is likely that atmospheric deposition is the
376 source of these elements. This is supported by work which has shown an increased
377 supply of dust in glacial periods during the past 2 myrs, variation which is clearly related
378 to Milankovitch periodicity (Kunkelova et al., 2018). Nitrogen in dust typically has a $\delta^{15}N$
379 value close to zero (Knapp et al., 2010) and therefore the values are consistent with the
380 data measured in this study. Regardless of the source of nutrients, enhanced
381 productivity should have resulted in more positive $\delta^{13}C$ values within the carbonate of the

dark layers. In fact, the carbonate within the darker layers possessed more negative $\delta^{13}C$ values compared to the light layers, suggesting the darker layers cannot be explained by higher productivity. There were no differences in the $\delta^{13}C_{TOC}$ values between the dark and light layers. Hence, the $\delta^{13}C$ values of both the organic and inorganic components tend to discount the enhanced productivity hypothesis as the major control on vaiability in TOC within the dark and light layers, although it may have been a contributing factor.

4.3. Preservation

An enhanced preservation origin of TOC within the dark layers implies that the bottom waters, present during the time that these layers were deposited, periodically became anoxic thus inhibiting degradation of organic material. This is supported by the higher concentrations of redox sensitive elements such as Mo, V, Th, Cr, and U within these organic-rich layers (Algeo and Lyons, 2006; Tribovillard et al., 2006). Under reducing conditions Mo, V, Cr, and others are quickly adsorbed by Fe and Mn-oxyhydroxides or incorporated into sulfides. As a consequence, while Modern anoxic basins show a high concentrations of these elements, they are also scavenged from the bottom waters, leading to an eventual depletion of the elements in poorly ventilated basins. Basins which are very restricted tend to have lower concentrations, than those basins with moderate restriction. This situation well exemplified by Mo which has been widely used as a paleoredox proxy (Algeo and Maynard, 2004; Piper, 1974; Sageman et al., 2003). Variations in the concentration of Mo relative to TOC was studied in a number of Modern anoxic basins, including the Cariaco Basin, the Black Sea, Franvaren Fjord, and Saanich

Inlet (Algeo and Lyons, 2006). These basins have sedimentary Mo/TOC ratios ranging from ~ 5 to 50 (x 10^{-4}). By comparison samples from the darker organic-rich layers of Core U1466-56R have Mo/TOC ratios of approximately 30, similar to those found in the Cariaco Basin and near the highest ratios found in Modern anoxic basins (Fig. 11). Using the correlation between Mo/TOC ratios presented by Algeo and Lyons (2006) would suggest a ventilation age of ancient inner sea of between 10 and 100 years, intermediary between basins such as the Black Sea (ventilation age> 500 years) and the Saanich Inlet (ventilation age < 2 years) (Algeo and Lyons, 2006).

Based on the variations in the concentrations of various trace elements, there appears to be evidence for enhanced productivity, driven probably by input of dust, as well as anoxia during the deposition of the dark layers. Such anoxic conditions could have arisen in response to sea-level changes, allowing the bottom waters in the basin to become isolated by virtue of a relatively shallow sill depth connecting the enclosed basin to the surrounding ocean. Similar control has been postulated for the organic-rich sediments in the Cariaco Basin (Peterson et al., 1991), and Black Sea (Lyons, 1991) and it is probably more than coincidental that the Mo/TOC ratios within the dark layers from core U1466-56R are similar to those found in the Cariaco Basin. A potential model of this mechanism in shown in Fig. 12. Support for this mechanism of sea-level variation driving restriction and enhanced organic matter preservation comes from other paleoceanographic indicators from this time. During the late Oligocene-Early Miocene changes in the volume of the Antarctic ice sheet produced variations of approximately 50m in sea level, well documented in the benthic (*Cibicides* sp.) oxygen isotope record (Liebrand et al., 2017;

Zachos et al., 2001). Such variation is also present in the $\delta^{18}O$ values of the carbonate fraction in Core U1466B-56R, which shows oscillations of about 1‰ between the dark and light layers. The changes in TOC tend to lag changes in the $\delta^{18}O$ values, as would be expected if sea level were a driving force in the preservation of TOC (Fig. 8). Sea level control of anoxia is also supported by the spectral analysis of the gamma ray and resistivity signals obtained from the logging. These reveal the presence of signals approximately coincident with tilt (40K) and eccentricity (100-120K) frequencies (Figs. 11 A & B). Higher gamma ray signals are predominantly a result of increases in the concentration of U which correspond to periods of bottom-water anoxia which formed during sea-level low stands. Similar spectral frequencies were noted in the Zachos et al. (2001) and Liebrand et al. (2017) datasets. The 20K frequency was not observed in this study because of the low spatial resolution of the logging tool relative to the rate of sediment deposition. We do not see a mechanism such as proposed for the production of sapropels in Mediterranean in which increased freshwater input was responsible for the development of anoxia (Emeis and Weissert, 2009; Rossignol-Strick, 1985). In the case of the Maldives there is no riverine source, such as in the Mediterranean, and therefore all the freshwater would have to be derived from rainwater. Not only would the volumes of water necessary be unrealistic, but this freshwater would cause the carbonate component to have more negative $\delta^{18}O$ values during the periods of dark layer formation, opposite to what is observed.

4.4 Changes during the deposition of the 'Dark and Light' Interval

Several observations shed light on the evolution of the light and dark sequences. First, the frequency of the alternations and variations in TOC were much greater in the older portion of the sequence suggesting that the isolation of the basin was much more effective during this time. Hence, later intervals did not experience the same degree of anoxia as evidenced by lighter shade of 'dark' layers (lower TOC) and the presence of burrows. At the same time the $\delta^{13}C_{TOC}$ values, while not showing significant changes between the dark and light layers, shows an increase from the bottom to the top of the dark and light interval (23.1 to 20 Ma) (Fig. 8 & 9). These more negative values may have originated from higher input of terrestrial material at bottom of the sapropel-bearing interval. Such an interpretation is supported by the relative distribution of short (C_{14}–C_{18}) and long (C_{24}–C_{32}) fatty acids (See supplemental material, Fig. S1-1 and S1-2) and changes in the C/N ratio of the TOC. The short chain fatty acids are mainly derived from aquatic organisms such as phytoplankton, while long ones are derived from higher plants (Cranwell, 1974; Ishiwatari et al., 2006; Meyers and Eadie, 1993). The trend within the dark and light intervals at Site U1466 shows a pronounced decrease from the bottom to the top of the interval. This may be a result of an increase in water depth from the late Oligocene to the Early Miocene meaning that the changes in sea level would be less effective in producing anoxia or alternatively a reduction in the magnitude of sea-level changes as suggested by the data of Liebrand et al. (2017). At Site U1468 there is a statistically significant decrease in the CN ratio in this interval, also interpretable as a reduction in the influence of terrestrial plants (Meyers and Eadie, 1993). At Site U1466, the C/N ratio is already close to the value expected for marine TOC throughout, and more positive $\delta^{13}C_{TOC}$ values compared to Site U1468 suggest that the site received less terrestrial TOC.

472

473 *4.6. Impact of Dark and Light Layers on Global Carbon Cycle*

474 Numerous studies have noted that there was globally an approximate 0.5 ‰ increase in
475 the $\delta^{13}C$ values of certain foraminifera coincident with the Oligocene-Miocene boundary
476 (Hodell and Woodruff, 1994; Liebrand et al., 2017; Woodruff and Savin, 1989; Wright and
477 Miller, 1992), although no specific carbon burial event has been identified that coincides
478 with this change. Whilst the direction and the timing of the change is consistent with the
479 increased burial of organic carbon noted in this paper, the amount of carbon theoretically
480 deposited in the Maldives during the time interval is insufficient to induce a global change
481 in the $\delta^{13}C$ value of seawater DIC of 0.5‰. However, it is possible that the phenomenon
482 of dark and light layers observed in the Maldives during this time was not unique and that
483 there were other systems, yet undocumented, where global sea level changes drove
484 similar changes in organic matter burial. For example, there is global wide increase of ~
485 0.3 ‰ in the $\delta^{13}C$ value of oceanic carbonates during the time represented by the
486 sapropels (Hodell and Woodruff, 1994; Woodruff and Savin, 1989). However, as an
487 increase of 0.3 ‰ in the $\delta^{13}C$ value of the oceans would require about a 4% increase in
488 the global burial rate of organic carbon it seems unlikely that the Maldives alone could not
489 account for the observed global change in $\delta^{13}C$ values. For example, if similar sapropels
490 were present in the Maldives at the same time, then the potential area available for these
491 to form would be ~45,000 km^2. Assuming that 50% of these strata were similar to the
492 dark layers found in this study and that they contained on average 10% organic carbon,
493 then the amount of buried organic carbon, based on a Berner type model (Berner et al.,
494 1983), would be approximately 100 times less than needed to account for the observed

change in the global $\delta^{13}C$ value and other therefore to account for the 0.3 ‰ change in $\delta^{13}C$ values other sites of organic accumulation must have been active at this time.

5.0 CONCLUSIONS

We have identified the presence of ~100 m thick sequences of organic-rich sediments (sapropels) alternating with organic poor oceanic carbonates in late-Oligocene and Early-Miocene strata in the Maldives Archipelago. The organic-rich components contain up to ~~30~~% organic carbon and have trace elements signatures characteristic of formation within anoxic bottom waters. These alternations occur within an atoll-like setting 1000 of meters above the surrounding ocean basin. Based on stable O and C isotopic variations within the carbonate components as well as spectral analysis of the NGR component of the logging data, we propose that these sapropels formed in response to the variations in orbitally induced sea-level fluctuations linked to Antarctic ice volume changes superimposed on a major transgression, which flooded a Late-Oligocene shallow-water carbonate platform. During the orbitally induced changes, the bottom waters within the atoll lagoon became anoxic and conducive to the preservation of organic material. As the water depth within the atoll became greater towards the end of the sapropels bearing interval, the isolation of the bottom water became less effective and the intensity of the sapropels diminished. While sea level induced ventilation has been proposed for the development of anoxia in closed basins such as the Cariaco Basin (Peterson et al., 1991) and Mediterranean (Emeis and Weissert, 2009) leading to the formation of sapropels, subtle changes in sea level might also be responsible for the formation of organic-rich

intervals within carbonate platform settings (Koster et al., 1988) as demonstrated in this study.

ACKNOWLEDGMENTS

The authors would like to thank the crew of the JOIDES Resolution. Analyses in Miami were supported by A. Saied. D. Houpt and M. Schoemann are acknowledged for assistance during XRF scanning at IODP Gulf Coast Repository. Support for MAG was provided by the Portuguese National Science and Technology Foundation (SFRH/BPD/96960/2013 and UID/Multi/04326/2013). Fatty acid analyses were supported by K. Takehara, S. Yamamoto, and the JAMSTEC post cruise research program. The SEM analyses were supported by the British Natural History Museum and funding from UKIODP. DK acknowledges support by the NERC (3148). Support for U.S. participants was provided by the IODP U.S. Science Support Office (NSF OCE1450528). Support for G. Mackenzie was provided by the Comparative Sedimentology Laboratory.

REFERENCES

Algeo, T.J., 2004. Can marine anoxic events draw down the trace element inventory of seawater? Geology 32, 1057-1060.

Algeo, T.J., Lyons, T.W., 2006. Mo-total organic carbon covariation in modern anoxic marine environments: Implications for analysis of paleoredox and paleohydrographic conditions. Paleocean. 21.

Algeo, T.J., Maynard, J.B., 2004. Trace-element behavior and redox facies in core shales of Upper Pennsylvanian Kansas-type cyclothems. Chem. Geol. 206, 289-318.

Altabet, M.A., Deuser, W.G., 1985. Seasonal variations in natural abundance of ^{15}N in particles sinking to the deep Sargasso Sea. Nature 315, 218-219.

Arthur, M.A., 1979. Paleoceanogrphic events-Recognition, resolution, and reconsideration Reviews of Geophysics 17, 1474-1494.

Aubert, O., Droxler, A.W., 1992. General Cenozoic evolution of the Maldives carbonate system (Equatorial Indian Ocean). Bulletin Des Centres De Recherches Exploration-Production Elf Aquitaine 16, 113-136.

Berner, R.A., Lasaga, A.C., Garrels, R.M., 1983. The carbonate-silicate geochemical cycle and its effect on atmospheric carbon dioxide over the past 100 million years. Am. J. Sci. 283, 641-683.

Betzler, C., Eberli, G.P., Kroon, D., Wright, J.D., Swart, P.K., Nath, B.N., Alvarez-Zarikian, C.A., Alonso-García, M., Bialik, O.M., Blättler, C.L., Guo, J.A., Haffen, S., Horozal, S., Inoue, M., Jovane, L., Lanci, L., Laya, J.C., Mee, A.L.H., Lüdmann, T., Nakakuni, M., Niino, K., Petruny, L.M., Pratiwi, S.D., Reijmer, J.J.G., Reolid, J., Slagle, A.L., Sloss, C.R., Su, X., Yao, Z., Young, J.R., 2016a. The abrupt onset of the modern South Asian Monsoon winds. Scientific Reports 6, 29838.

Betzler, C., Eberli, G.P., Lüdmann, T., Reolid, J., Kroon, D., Reijmer, J.J.G., Swart, P.K., Wright, J., Young, J.R., Alvarez-Zarikian, C., Alonso-García, M., Bialik, O.M., Blättler, C.L., Guo, J.A., Haffen, S., Horozal, S., Inoue, M., Jovane, L., Lanci, L., Laya, J.C., Hui Mee, A.L., Nakakuni, M., Nath, B.N., Niino, K., Petruny, L.M., Pratiwi, S.D., Slagle, A.L., Sloss, C.R., Su, X., Yao, Z., 2018. Refinement of Miocene sea level and monsoon events from the sedimentary archive of the Maldives (Indian Ocean). Progress in Earth and Planetary Science 5, 5.

Betzler, C., Eberli, G.P., Zarkian, C., Shipboard Scientific Party, 2016b. Proceedings of the Initial Results of Expedition 359. IODP, College Station.

Bohacs, K.M., 2005. Production, destruction, and dilution-The many paths to source-rock development, The Deposition of Organic-Carbon-Rich Sediments: Models, Mechanisms, and Consequences. Society for Sedimentary Geology, Tulsa, pp. 17–33.

Boyle, E.A., 1981. Cadmium, zinc, copper, and barium in foraminifera tests. Earth Planet. Sci. Lett. 53, 11-35.

Brumsack, H.J., 2006. The trace metal content of recent organic carbon-rich sediments: Implications for Cretaceous black shale formation. Palaeogeography, Palaeoclimatology, Palaeoecology 232, 344-361.

Coplen, T.B., Brand, W.A., Gehre, M., Groning, M., Meijer, H.A.J., Toman, B., Verkouteren, R.M., 2006. After two decades a second anchor for the VPDB $\delta^{13}C$ scale. Rapid Commun. Mass Spectrom. 20, 3165-3166.

Cranwell, P.A., 1974. Monocarboxylic acis in lake sediments-Indicators derived from terrestrial and aquatic biota of paleoenvironmental trophic levels. Chem. Geol. 14, 1-14.

Davis, J.C., 1973. Statistics and Data Analysis in Geology. Wiley, New York.

Duncan, R.A., Hargraves, R.B., 1990. $^{40}Ar/^{39}Ar$ geochronology of basement rocks from the Mascarene Plateau, the Chagos Bank, and the Maldives Ridge, in: Duncan, R.A., Backman, J., Peterson, L.C. (Eds.), Proceedings of the Ocean Drilling Program, Scientific Results,. Ocean Drilling Program, College Station, pp. 43-51.

578 Emeis, K.-C., Weissert, H., 2009. Tethyan–Mediterranean organic carbon-rich sediments from Mesozoic
579 black shales to sapropels. Sedimentology 56, 247-266.
580 Gardner, R.D., Pope, M.C., Wehner, M.P., Donovan, A.D., 2013. Comparative stratigraphy of the Eagle
581 Ford group strata in Lozier Canyon and Antoniio Creek, Terrell County, Texas. Gulf Coast Association of
582 Geological Societies, Journal 2, 42-52.
583 Govindaraju, K., 1994. 1994 Compilation of working values and sample description for 383
584 geostandards. 18, 1-158.
585 Hodell, D.A., Woodruff, F., 1994. Variations on the strontium isotopic ratio of seawater during the
586 Miocene- Stratigraphi and geochemical inplications. Paleocean. 9, 405-426.
587 Ishiwatari, R., Yamamoto, S., Shinoyama, S., 2006. Lignin and fatty acid records in Lake Baikal sediments
588 over the last 130 kyr: A comparison with pollen records. Org. Geochem. 37, 1787-1802.
589 Jenkyns, H.C., 2010. Geochemistry of oceanic anoxic events. Geochem. Geophys. Geosys. 11.
590 Knapp, A.N., Hastings, M.G., Sigman, D.M., Lipschultz, F., Galloway, J.N., 2010. The flux and isotopic
591 composition of reduced and total nitrogen in Bermuda rain. Mar. Chem. 120, 83-89.
592 Koster, J., Wehner, H., Hufnagel, H., 1988. Organic geochemistry and organic petrology of organic-rich
593 sediments within the main dolomite formation (Triassic, Nornian) of the northern calcreous Alps. Org.
594 Geochem. 13, 377-386.
595 Kunkelova, T., Jung, S.J.A., de Leau, E.S., Odling, N., Thomas, A.L., Betzler, C., Eberli, G.P., Alvarez-
596 Zarikian, C.A., Alonso-García, M., Bialik, O.M., Blättler, C.L., Guo, J.A., Haffen, S., Horozal, S., Mee, A.L.H.,
597 Inoue, M., Jovane, L., Lanci, L., Laya, J.C., Lüdmann, T., Bejugam, N.N., Nakakuni, M., Niino, K., Petruny,
598 L.M., Pratiwi, S.D., Reijmer, J.J.G., Reolid, J., Slagle, A.L., Sloss, C.R., Su, X., Swart, P.K., Wright, J.D., Yao,
599 Z., Young, J.R., Lindhorst, S., Stainbank, S., Rueggeberg, A., Spezzaferri, S., Carrasqueira, I., Hu, S., Kroon,
600 D., 2018. A two million year record of low-latitude aridity linked to continental weathering from the
601 Maldives. Progress in Earth and Planetary Science 5, 86.
602 Lea, D.W., Boyle, E.A., 1991. Barium in planktonic foraminifera. Geochim. Cosmochim. Acta 55, 3321-
603 3331.
604 Liebrand, D., de Bakker, A.T.M., Beddow, H.M., Wilson, P.A., Bohaty, S.M., Ruessink, G., Palike, H.,
605 Batenburg, S.J., Hilgen, F.J., Hodell, D.A., Huck, C.E., Kroon, D., Raffi, I., Saes, M.J.M., van Dijk, A.E.,
606 Lourens, L.J., 2017. Evolution of the early Antarctic ice ages. Proc. Natl. Acad. Sci. U. S. A. 114, 3867-
607 3872.
608 Lyons, T.W., 1991. Upper Holocene sediments of the Black Sea: summary of Leg 4 box cores (1988 Black
609 Sea oceanographic expedition), in: Izdar, E., Murray, J.W. (Eds.), Black Sea Oceanography. Kluwer
610 Academic Publishers, Netherlands, pp. 401-441.
611 Meyers, P.A., Eadie, B.J., 1993. Sources , degradation and recyling of organic matter associated with
612 sinking particles in Lake Michigan. Org. Geochem. 20, 47-56.
613 Miller, K.G., Mountain, G.S., Wright, J.D., Browning, J.V., 2011. A 180-Million-Year Record of Sea Level
614 and Ice Volume Variations from Continental Margin and Deep-Sea Isotopic Records. Oceanography 24,
615 40-53.
616 Mutti, M., Bernoulli, D., Stille, P., 1997. Temperate carbonate platform drowning linked to Miocene
617 oceanographic events: Maiella platform margin, Italy. Terra Nova 9, 122-125.
618 Oehlert, A.M., Lamb-Wozniak, K.A., Devlin, Q.B., Mackenzie, G.J., Reijmer, J.J.G., Swart, P.K., 2012. The
619 stable carbon isotopic composition of organic material in platform derived sediments: implications for
620 reconstructing the global carbon cycle. Sedimentology 59, 319-335.
621 Parrish, J.T., Curtis, R.L., 1982. Atmospheric circulation, upwelling, and organic-rich rocks in the
622 Mesozoic and Cenozoic eras Palaeo. Palaeo. Palaeo. 40, 31-66.
623 Peterson, L.C., Overpeck, J.T., Kipp, N.G., Imbrie, J., 1991. A high-resolution late Quaternary upwelling
624 record from the anoxic Cariaco Basin, Venezuela. Paleocean. 6, 99-119.
625 Piper, D.Z., 1974. Rare Earth elements in the sedimentary cycle: a summary. Chem. Geol. 14, 285-304.

626 Reolid, J., Betzler, C., 2018. Ichnofabric logs for the characterization of the organic content in
627 carbonates. Marine and Petroleum Geology 95, 246-254.
628 Reynolds, R.C., 1963. Matrix correlations in trace element analysis by X-ray fluorescence-Estimation of
629 mass absorption coefficient by compton scattering Am. Mineral. 48, 1133-&.
630 Rossignol-Strick, M., 1985. Mediterranean Quaternary sapropels, an immediate response of the African
631 Monsoon to variation of insolation. Palaeogeography, Palaeoclimatology, Palaeoecology 49, 237-263.
632 Sageman, B.B., Murphy, A.E., Werne, J.P., Straeten, C.A.V., Hollander, D.J., Lyons, T.W., 2003. A tale of
633 shales: the relative roles of production, decomposition, and dilution in the accumulation of organic-rich
634 strata, Middle-Upper Devonian, Appalachian basin. Chem. Geol. 195, 229-273.
635 Schlanger, S.O., Jenkyns, H.C., 1976. Cretaceous anoxic events: Causes and consequences. Geologie en
636 Mijnbouw 55, 179-184.
637 Tribovillard, N., Algeo, T.J., Lyons, T., Riboulleau, A., 2006. Trace metals as paleoredox and
638 paleoproductivity proxies: An update. Chem. Geol. 232, 12-32.
639 Woodruff, F., Savin, S.M., 1989. Miocene deepwater oceanography. Paleocean. 4, 87-140.
640 Wright, J., Miller, K., 1992. Miocene stable isotope stratigraphy, Site 747, Kerguelan Plateau in: Schlich,
641 R., Wise, S.W., Jr., Palmer-Julson, A. (Eds.), Proceedings of Ocean Drilling Program Scientific Results,
642 College Station, pp. 855-866.
643 Zachos, J.C., Pagani, M., Sloan, L., Thomas, E., Billups, K., 2001. Trends, rhythms, and aberrations in
644 global climate 65 Ma to present. Science 292, 686-693.

645

FIGURE CAPTIONS

Figure 1: A) Map showing the location of Sites U1466 and U1468 drilled during IODP Expedition 359. B) Seismic line showing the location and depth of penetration of Sites U1466 and U1468.

Figure 2: Core photograph of dark and light layers from A) U1466B-56R-1 & 2, and B) U1468A-105X-1.

Figure 3: Facies and components of the dark and light layers. A) Close-up and B) photomicrograph of a dark layer at 790.8 mbsf at Site U1466 (U1466B-56R-1W-117) showing a wackestone with trace fossils (*Phycosiphon*-Ps, *Planolites*-Pl, and *Thalassinoides*-Th) and allochems (fish bones-FB, planktonic foraminifera-PF, and organic matter-TOC). C) Close-up and D) photomicrograph of a light interval at 806.960 mbsf at Site U1468 (U1468A-105X-1W-76) displaying a wackestone with a burrow of *Palaeophycus* (Pa), and common planktonic foraminifera (PF).

Figure 4: Scanning electron micrographs of fracture surfaces of sediment samples from a pair of light-dark levels with particularly good nannofossil preservation.

A, B) Dark layer, sample U1466B-56R-1W 45cm. The dominant coccolith is *Cyclagelosphaera floridana*, including several coccospheres, *Sphenolithus disbelemnos* is also common (conical nannoliths with honeycomb-like fabric).

C, D) Light layer, sample U1466B-56R-1W 35cm. The dominant coccoliths are *Cyclagelosphaera floridana* (larger circular coccoliths) and *Umbilicosphaera jafari* (smaller circular coccoliths), note also strongly overgrown specimens of *Discoaster deflandrei* (lower right in D).

Figure 5: Changes in the percent organic content, $\delta^{13}C_{OM}$, $\delta^{15}N$ and C/N ratio between 700 and 800 mbsf from U1466 plotted against age. Also shown are the compilation of benthic $\delta^{18}O$ values for the same time period from Zachos et al. (2001).

Figure 6: Changes in the percent organic content, $\delta^{13}C_{OM}$, $\delta^{15}N$, C/N ratio and NGR (logging data) between 700 and 800 mbsf from U1468.

Figure 7: Changes in the concentration of nutrients like elements (Cd and Ba), detrital elements (Fe and Al), and Redox elements (Mo, V, Th, and U)determined by ICP-MS compared to the percentage of organic carbon, the $\delta^{18}O$ and $\delta^{13}C$ values of the carbonate and the $\delta^{15}N$ values measured in the TOC in U1466B-56R-1. The solid line in each graph represents a three-point moving average. All metal concentrations in ppm.

686

687 Figure 8: XRF data from U1466B-56R-1 showing the variation in redox, dust, nutrient,
688 and organic related elements relative to the TOC and the dark and light layers.
689 Concentration units for all elements are in counts per second.

690

691 Figure 9: XRF data from U1468A-105x-1 showing the variation in redox and dust related
692 elements associated with the dark and light layers. Concentration units for all elements
693 are in counts per second.

694

695 Figure 10: A) Spectral analysis of natural gamma data obtained from the logging run at
696 Site U1468 between a depth of 700 and 800 mbsf. B) Spectral analysis of resistivity data
697 from the logging run at Site U1468 between a depth of 700 and 800 mbsf. For both
698 gamma and resistivity age assignments have been made using shipboard biostratigraphy
699 and have been interpolated to a time interval of 10,000 years.

700

701 Figure 11: Data from Core U146656R show the relationship between the concentration
702 of Mo and the TOC (red symbols) relative to similar data published by Algeo and Lyons
703 (2006) from the Black Sea and Saanich Inlet. Data for the dark intervals are highlighted
704 in the oval while the light layers have values of Mo and TOC close to zero.

705

706 Figure 12: A cartoon demonstrating how sea level changes could lead to the development
707 of anoxia. In the upper panel the inter-atoll basin is connected to the surrounding ocean
708 and water flows freely into the basin. In the lower panel, sea level has fallen and access
709 to the basin become restricted leading to the development of anoxia.

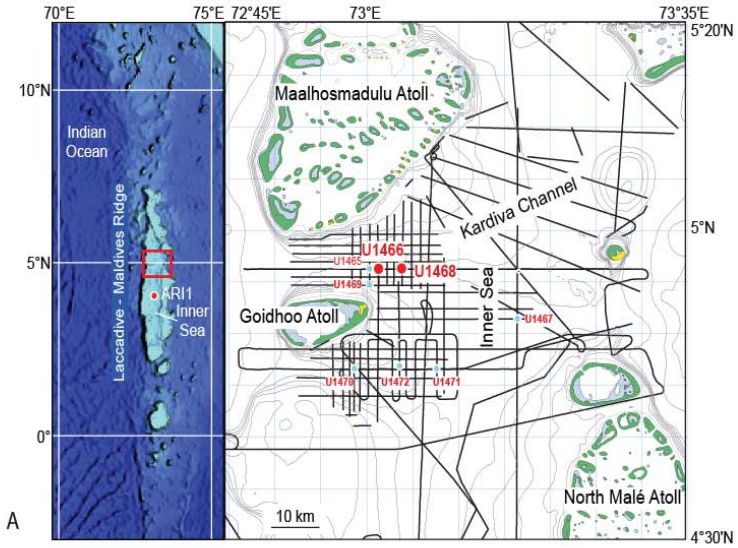
70°E
75°E
72°45'E
73°E
73°35'E
5°20'N
10°N
5°N
0°
4°30'N
Indian Ocean
Laccadive - Maldives Ridge
ARI1
Inner Sea
Maalhosmadulu Atoll
Kardiva Channel
U1466
U1465
U1468
U1469
Goidhoo Atoll
Inner Sea
U1467
U1470
U1472
U1471
North Malé Atoll
10 km
A

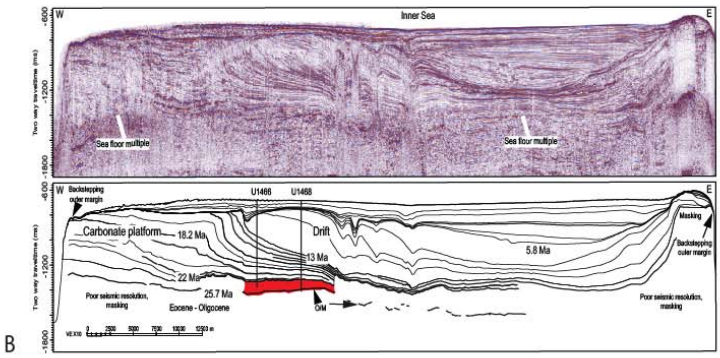
W
Inner Sea
E
Sea floor multiple
Sea floor multiple
Backstepping outer margin
U1466
U1468
Carbonate platform
18.2 Ma
Drift
13 Ma
22 Ma
25.7 Ma
5.8 Ma
Masking
Backstepping outer margin
Poor seismic resolution, masking
Eocene - Oligocene
CRM
Poor seismic resolution, masking
B

710

Figure 2

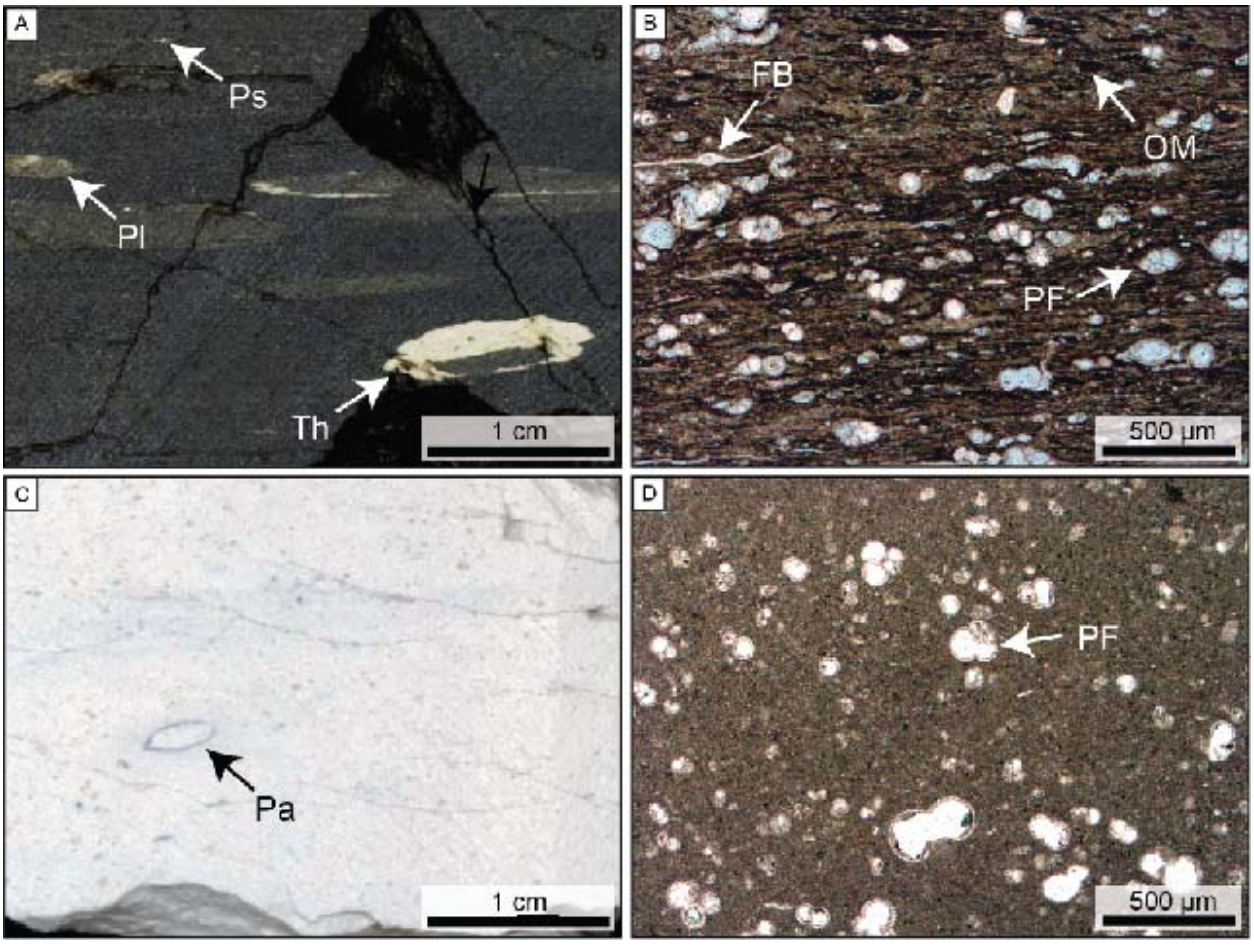

Figure 3

715

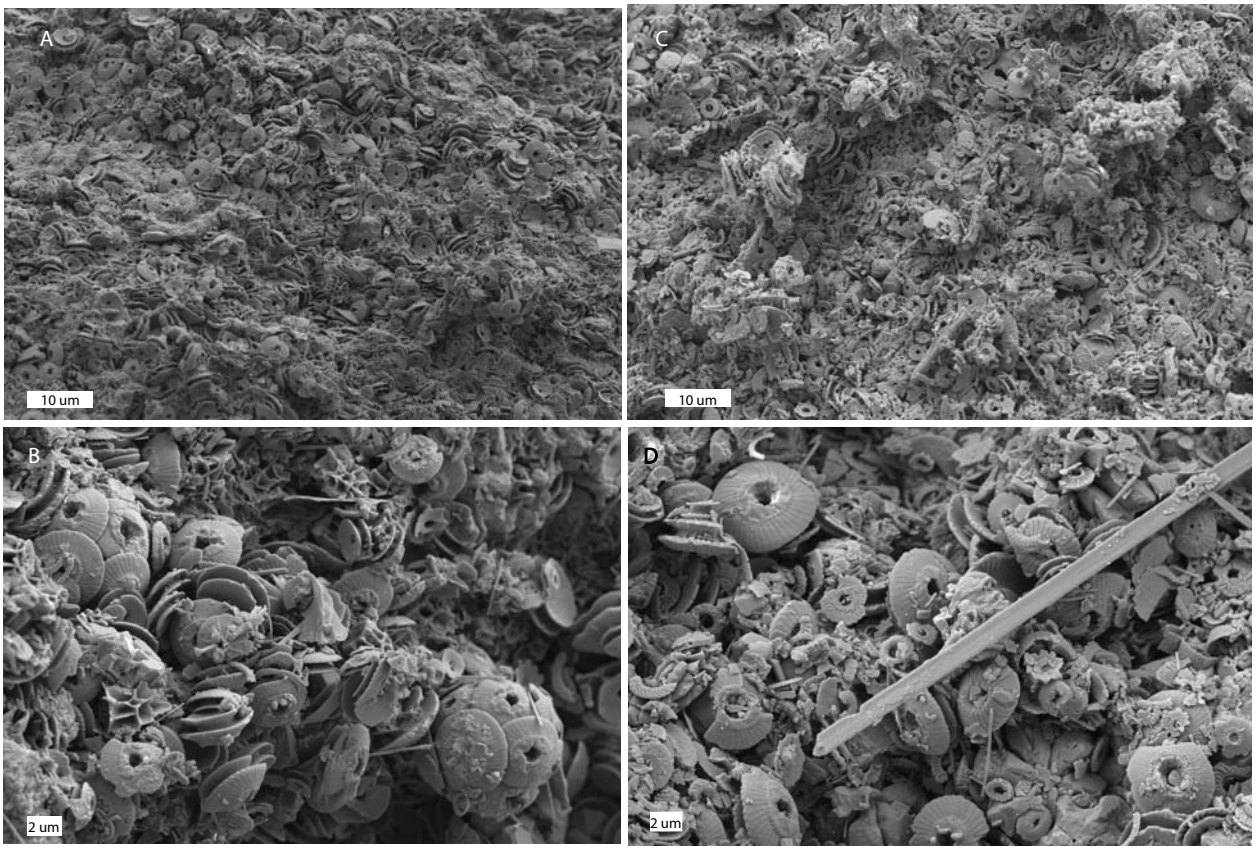

716 A and B) U1466A-56x-1-45 (Black Layer) C and D) U1466A-56x-1-35 (White Layer)

717 Figure 4

718

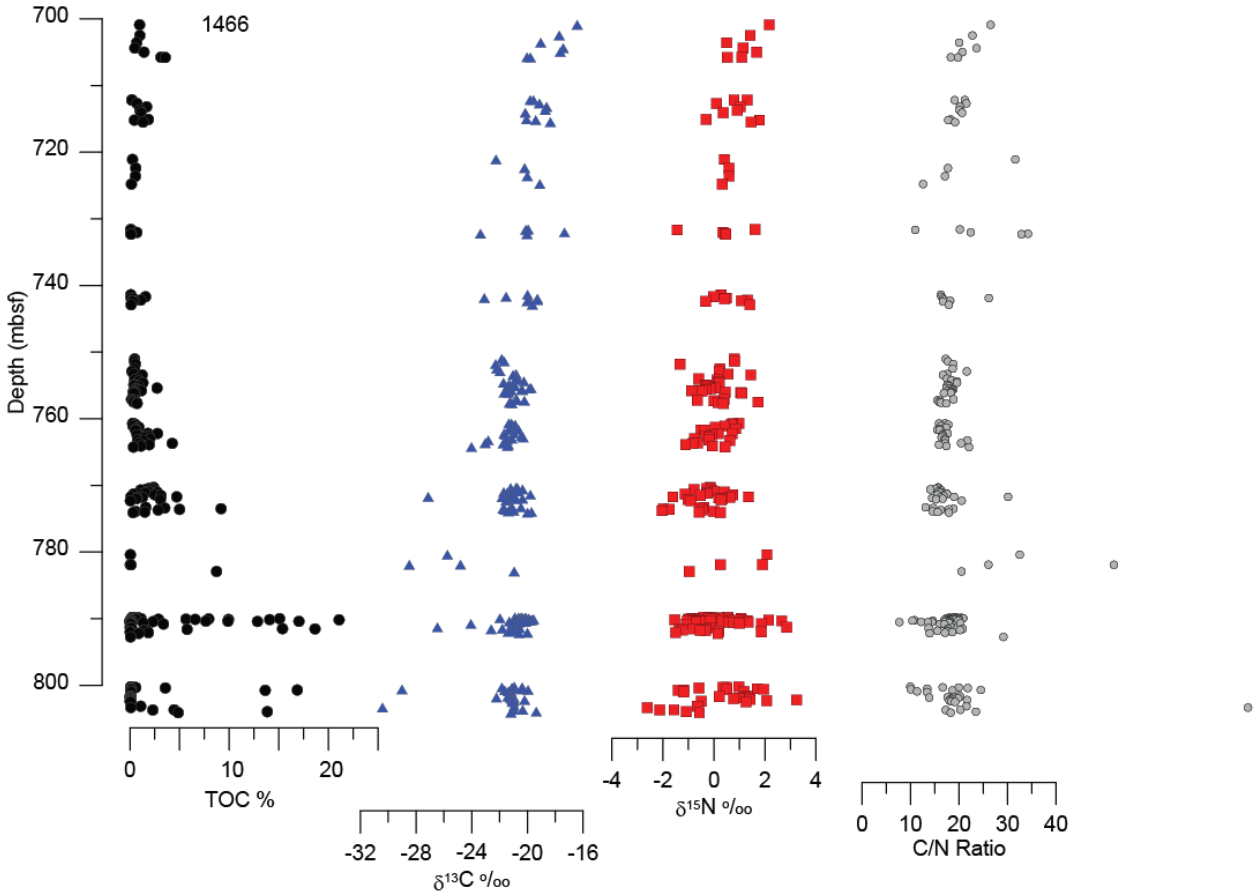

719

720 Figure 5

721

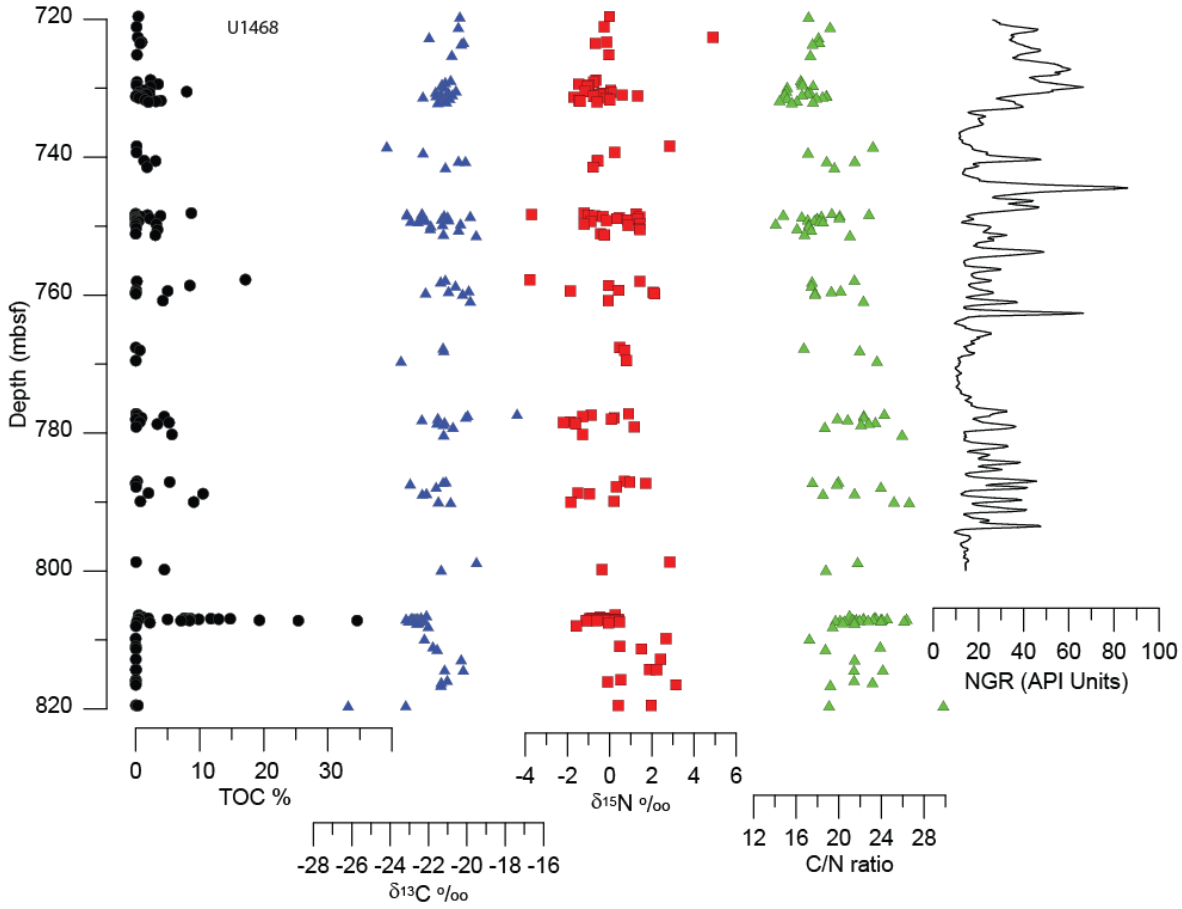

722

723 Figure 6

724

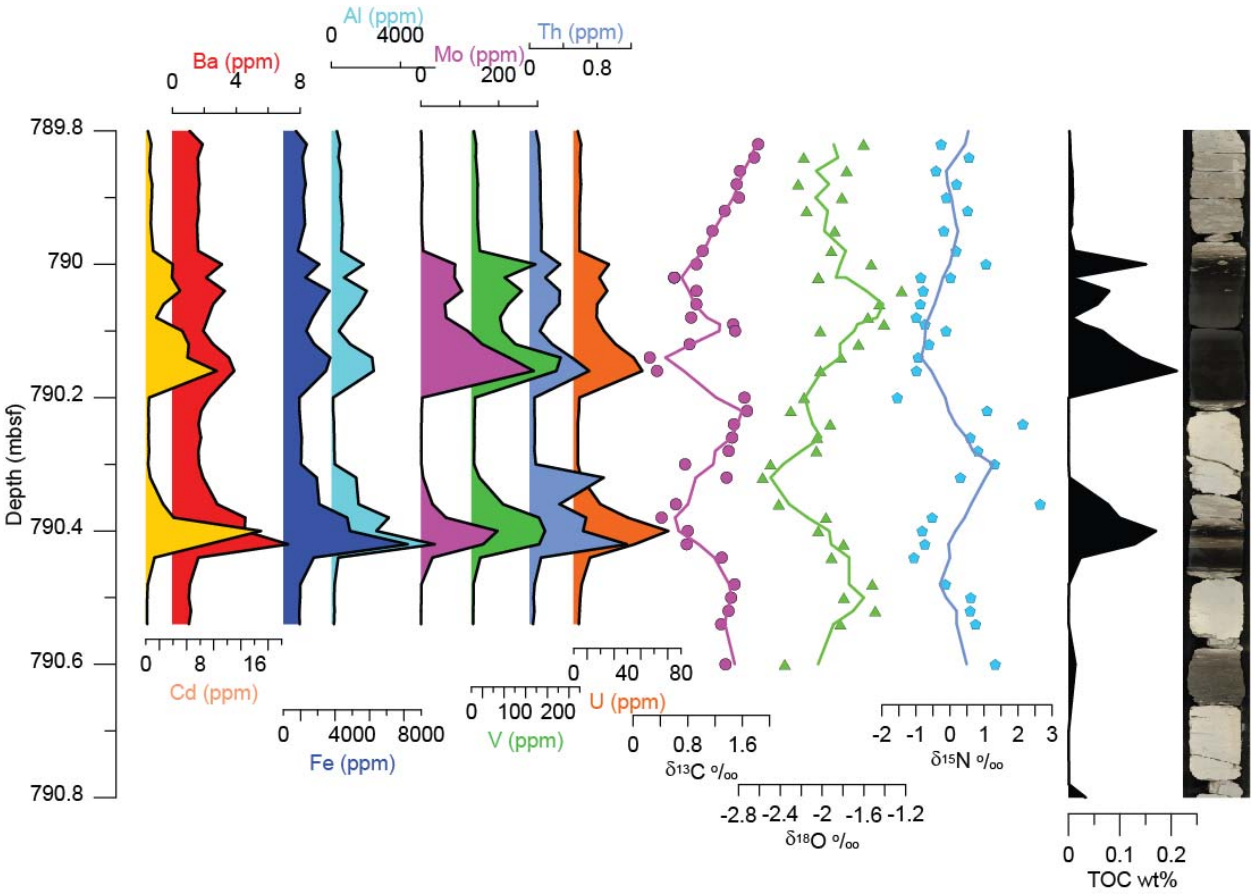

725

726

727 Figure 7

728

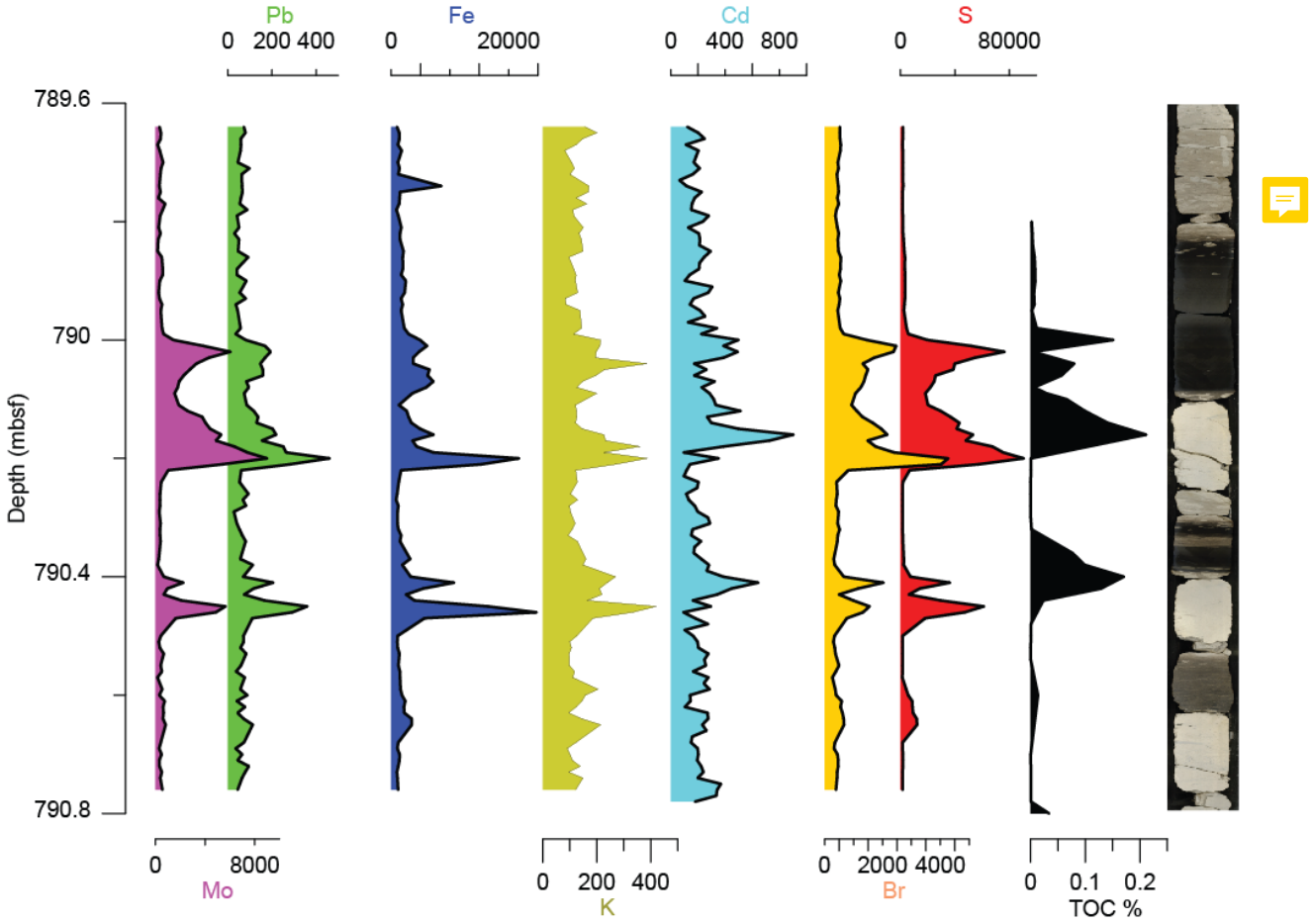

729

730 Figure 8

731

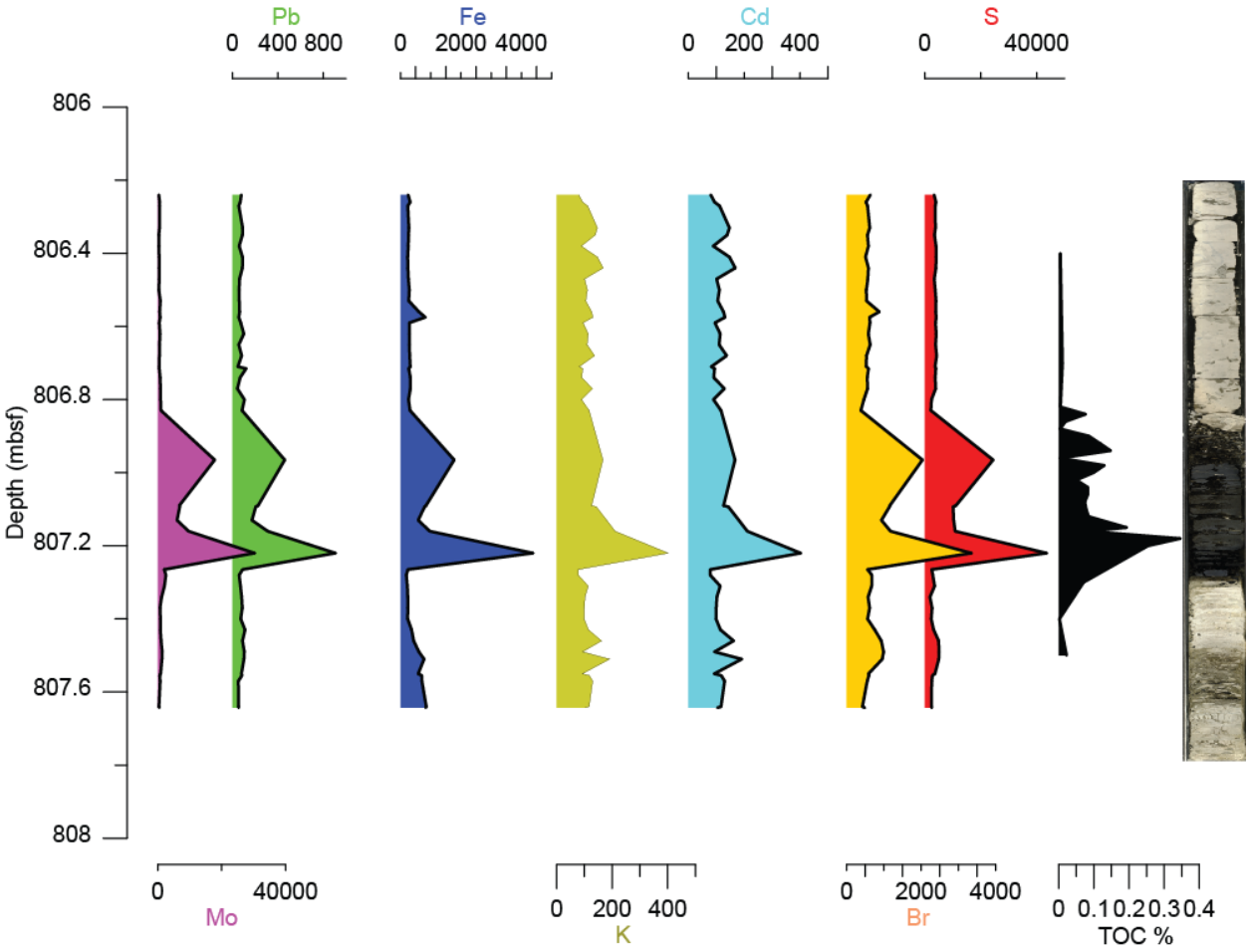

732

733

734 Figure 9

735

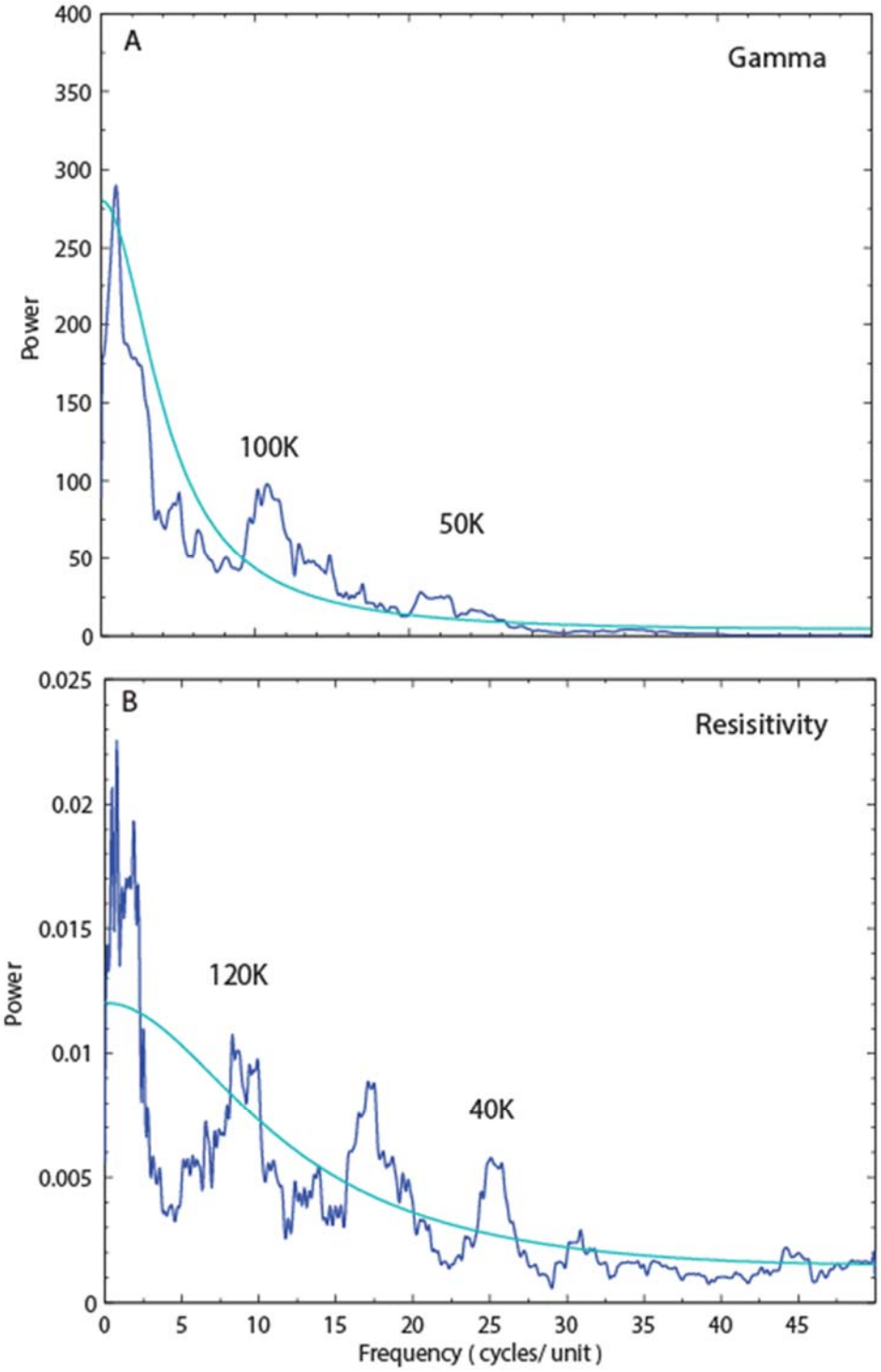

736

737 Figure 10

738

739

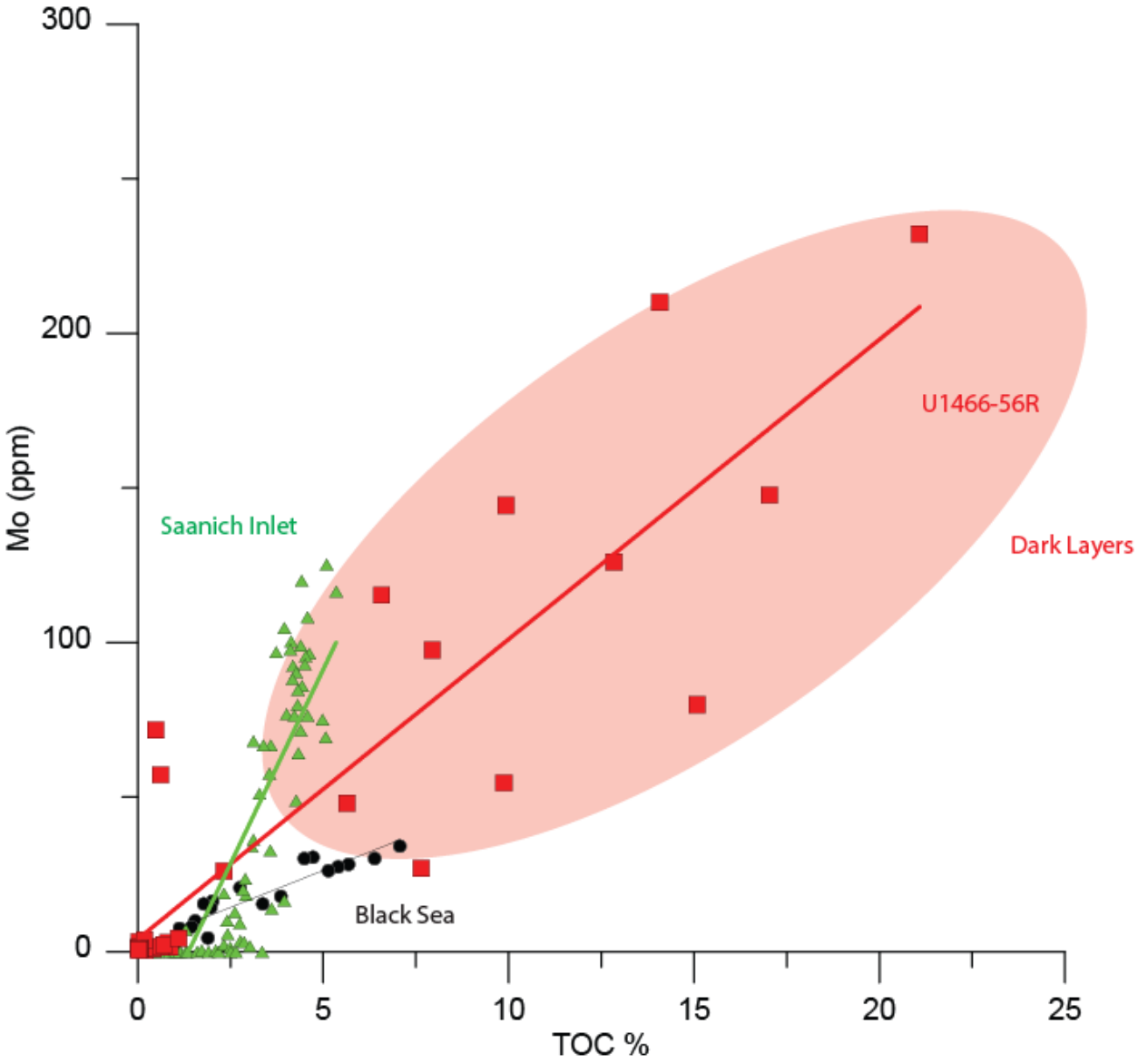

740

741 Figure 11

742

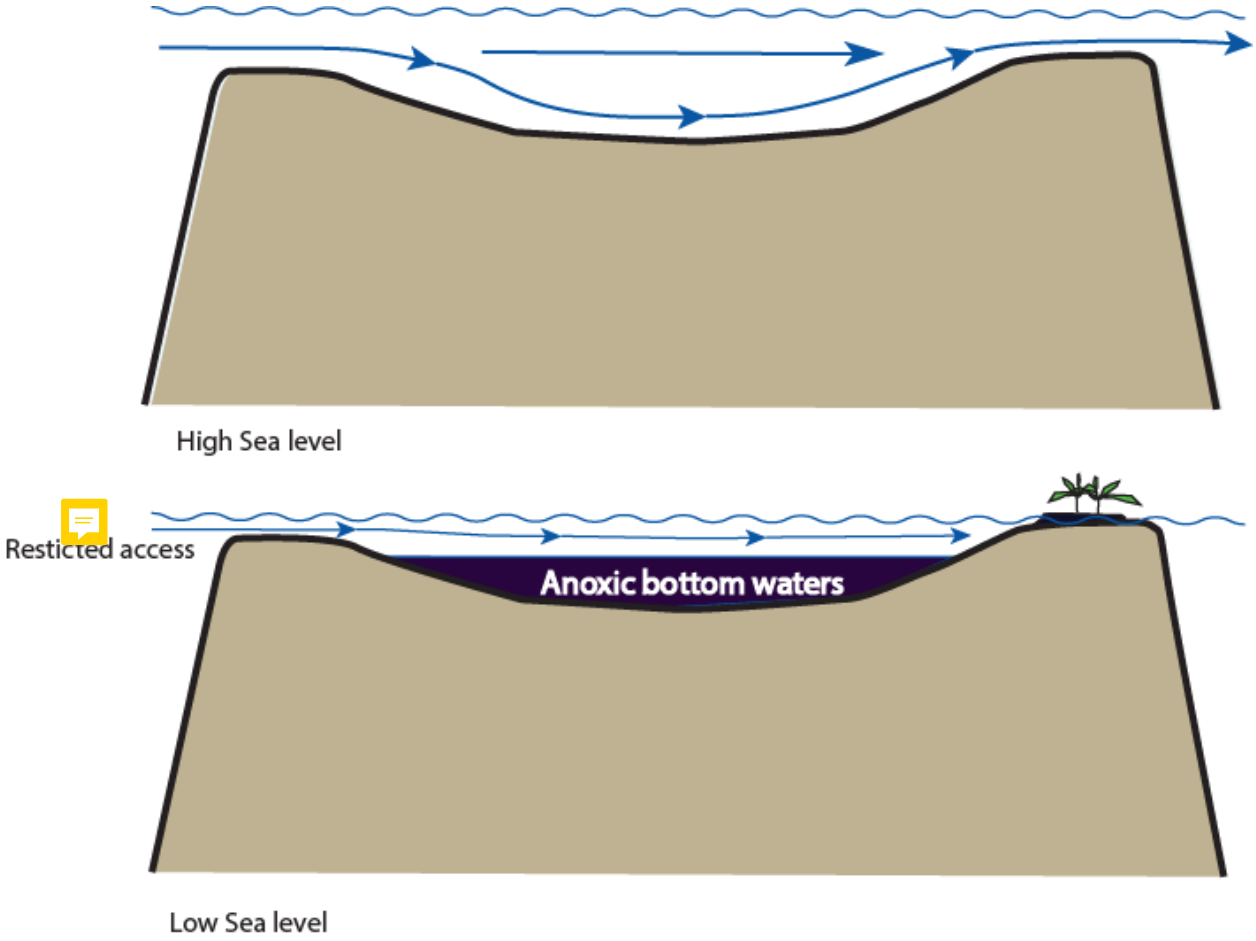

743

744

745 Figure 12

746

Supplemental Material S1: Organic Geochemistry

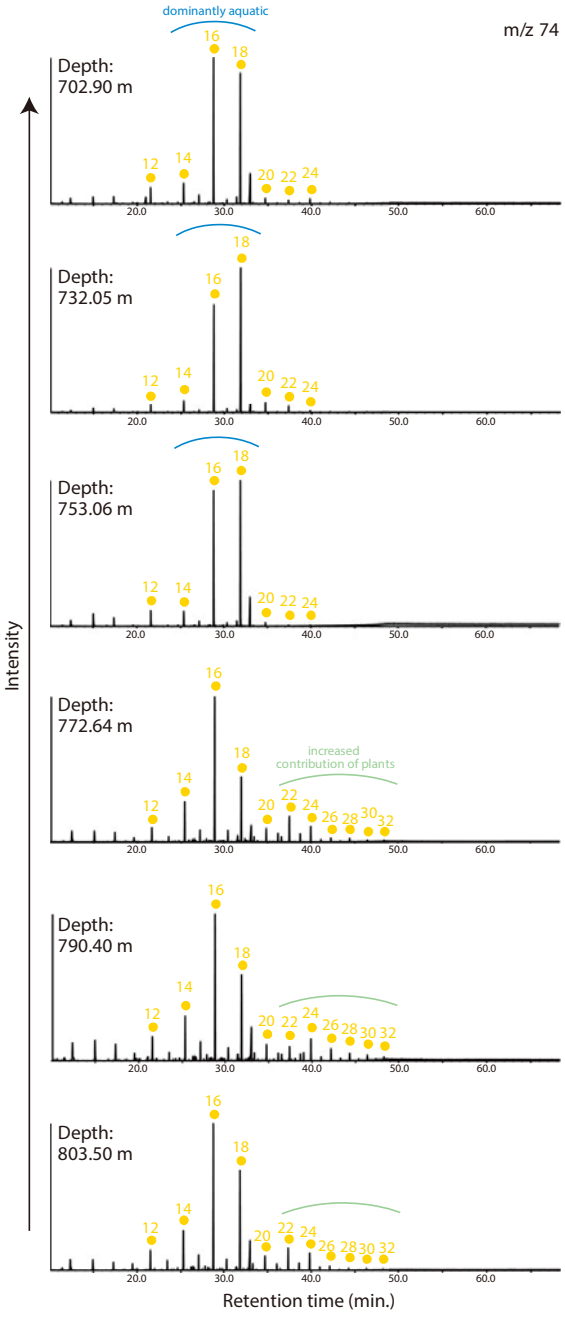

Figure S1-1: Representative mass fragmentograms (*m*/*z* 74) of fatty acids in the Maldives sediment (U1466) between 702.9 and 803.5 mbsf. Circles and each number denote fatty acids and carbon atom number, respectively.

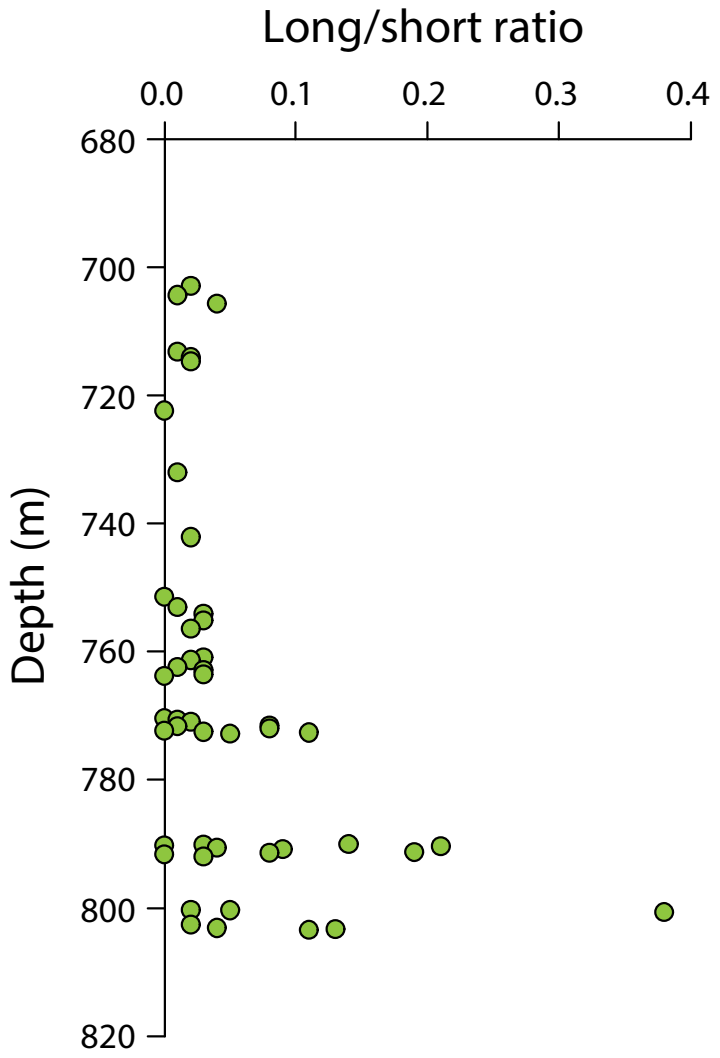

Figure S1-2: Vertical profiles of *n*-C_{22}–C_{32} fatty acids to *n*-C_{14}–C_{32} fatty acids (long/short) ratio from U1466 between 702.9 and 803.5 mbsf. Long/short ratio; $(C_{24}+C_{26}+C_{28}+C_{30}+C_{32})/(C_{14}+C_{16}+C_{18})$.

Supplemental Material S2: Correlation between XRF and ICP-MS data

Samples for the ICP-MS were taken every 2 cms from Core 1466B-56R-1A and analyzed using the methods described in the accompanying paper. The XRF measurement were made on the archive half of the core at an interval of 1 cm. There were nine elements measured using both methods. Note that elements which gave negative counts using the scanning XRF were not compared. For comparison of the intensity data from the XRF with the ICP-MS data, the XRF data were interpolated to a sample interval of 2cm using a rectangular interpolation method adapted from Davis (1973). The data were then compared using a Pearson regression coefficient. As a result of the fact that the cores were not completed filled, there was the possibility that the depth in the archive and working portions of the core were different. For this reason the correlation between the XRF and ICP-MS data was subject to a lag analysis to determine the optimum correlation. The correlation coefficients are shown in Table S1. With the exception of Cr all showed positive covariance between the XRF and ICP-MS measurements. Generally there was about a 2-4 cm mismatch between the working and archive halves of the cores.

	0	2 cm	4 cm
Fe	0.17	0.36	0.67
Sr	0.26	0.36	0.28
Mo	0.40	0.74	0.51
Pb	0.05	0.37	0.28
Cr	-ve	-ve	-ve
Ba	0.02	0.16	0.13
Al	0.06	0.27	0.47
Mg	0.06	0.15	0.21
Cd	0.21	0.43	0.06

Table S1-1: R^2 values between XRF and ICPMS analyses as a function of lags. Those in red are statistically significant at the 99% confidence limits.

Further discrepancy between the two measurements arises as a result of nature of the analysis. The XRF technique targets the entire sample, including acid soluble and insoluble components, while the ICP-MS only analyzes the acid soluble portion plus any elements leached from the acid insoluble component. In addition the core is often heterogeneous in composition and the ICP-MS only analyses a small portion of the core while the XRF integrates signals from a much larger region. Consequently the concentrations measured by ICP-MS can be considered a minimum value. This differential leaching probably accounts for the discrepancies in the lag analysis which suggests different components were leached during the ICPMS analyses in different intervals. The absence of a correlation between Ba, Cr Mg and Cd probably results from low detection limits of the XRF.

References

Davis, J.C., 1973. Statistics and Data Analysis in Geology. Wiley, New York.

Kunkelova, T., Jung, S.J.A., de Leau, E.S., Odling, N., Thomas, A.L., Betzler, C., Eberli, G.P., Alvarez-Zarikian, C.A., Alonso-García, M., Bialik, O.M., Blättler, C.L., Guo, J.A., Haffen, S., Horozal, S., Mee, A.L.H., Inoue, M., Jovane, L., Lanci, L., Laya, J.C., Lüdmann, T., Bejugam, N.N., Nakakuni, M., Niino, K., Petruny, L.M., Pratiwi, S.D., Reijmer, J.J.G., Reolid, J., Slagle, A.L., Sloss, C.R., Su, X., Swart, P.K., Wright, J.D., Yao, Z., Young, J.R., Lindhorst, S., Stainbank, S., Rueggeberg, A., Spezzaferri, S., Carrasqueira, I., Hu, S., Kroon, D., 2018. A two million year record of low-latitude aridity linked to continental weathering from the Maldives. Progress in Earth and Planetary Science 5, 86.

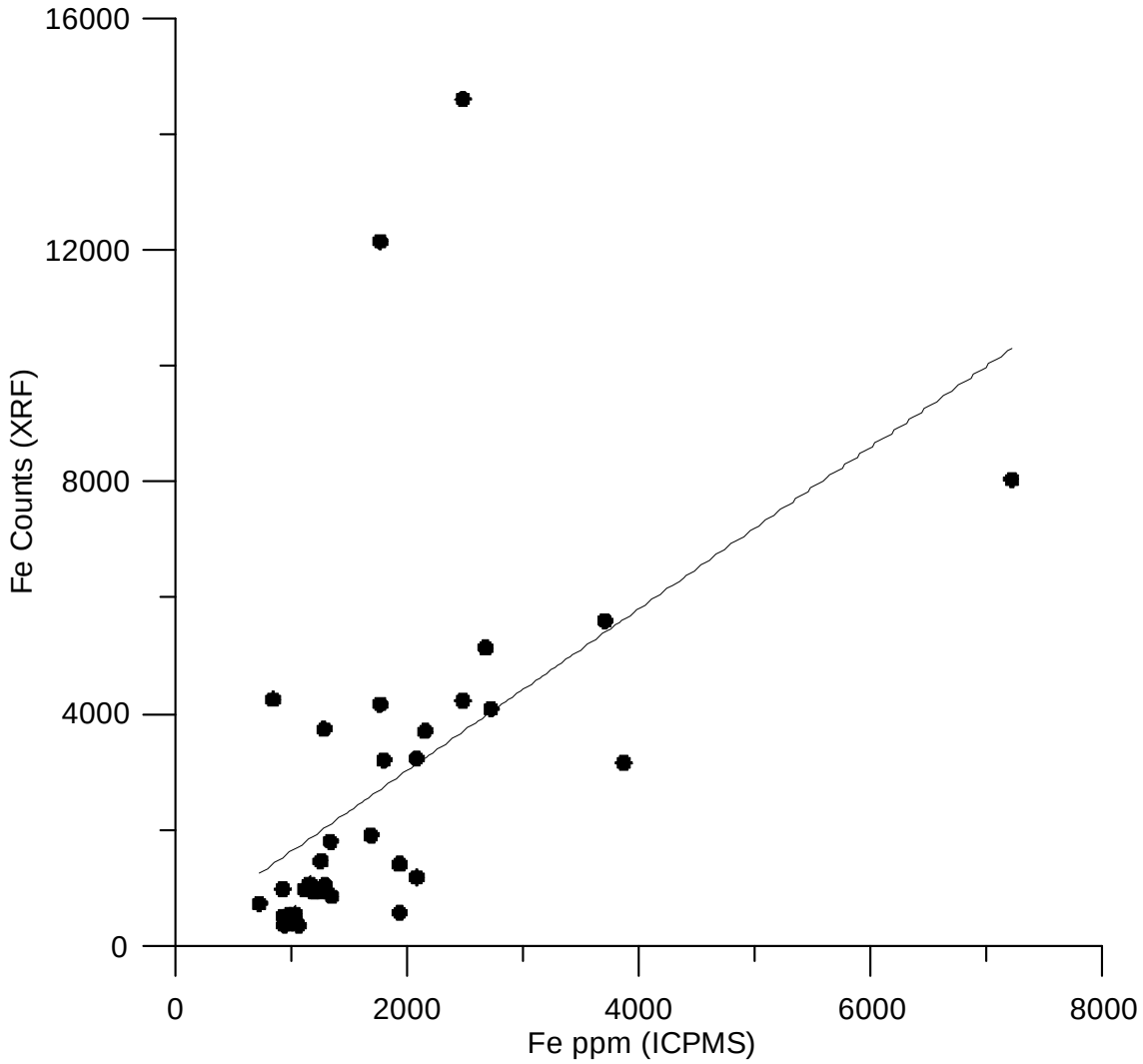

Figure S2-1: Comparison of concentration of Fe measured using ICPMS with the intensity derived from the XRF at a lag of 2 cm between working and archive halves of the core.

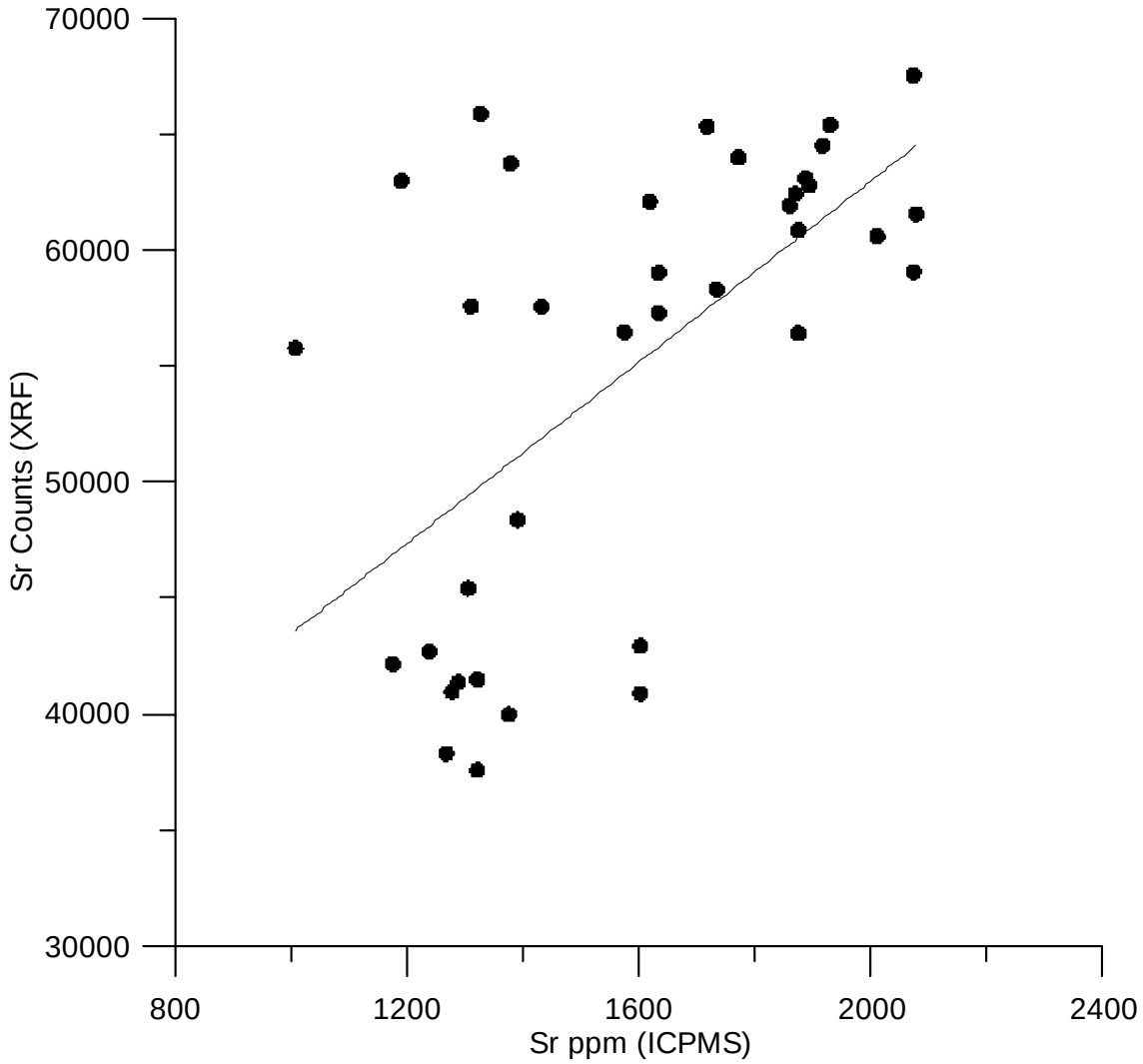

Figure S2-2: Comparison of concentration of Sr measured using ICPMS with the intensity derived from the XRF at a lag of 2 cm between working and archive halves of the core.

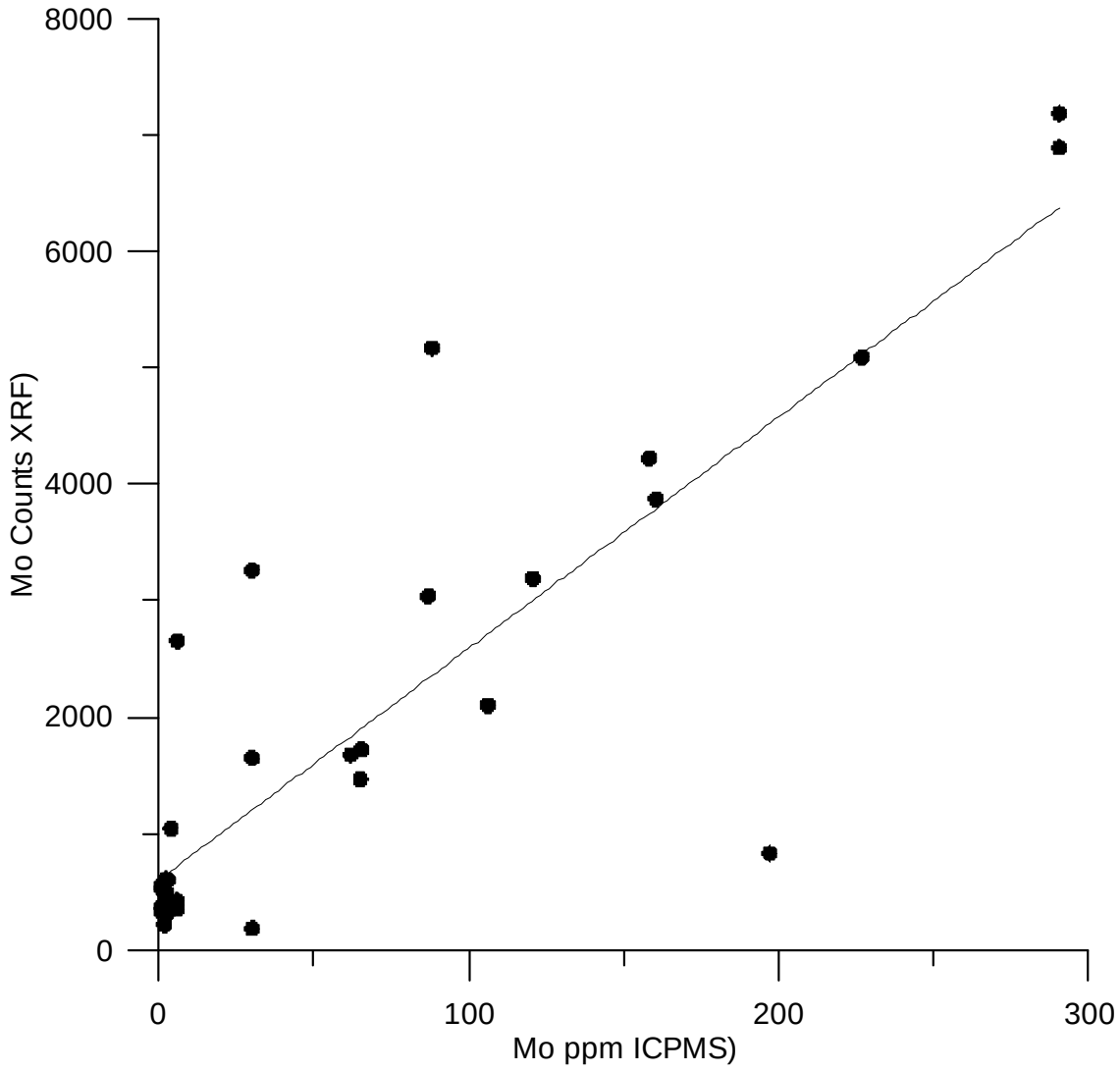

Figure S2-3: Comparison of concentration of Mo measured using ICPMS with the intensity derived from the XRF at a lag of 2 cm between working and archive halves of the core.

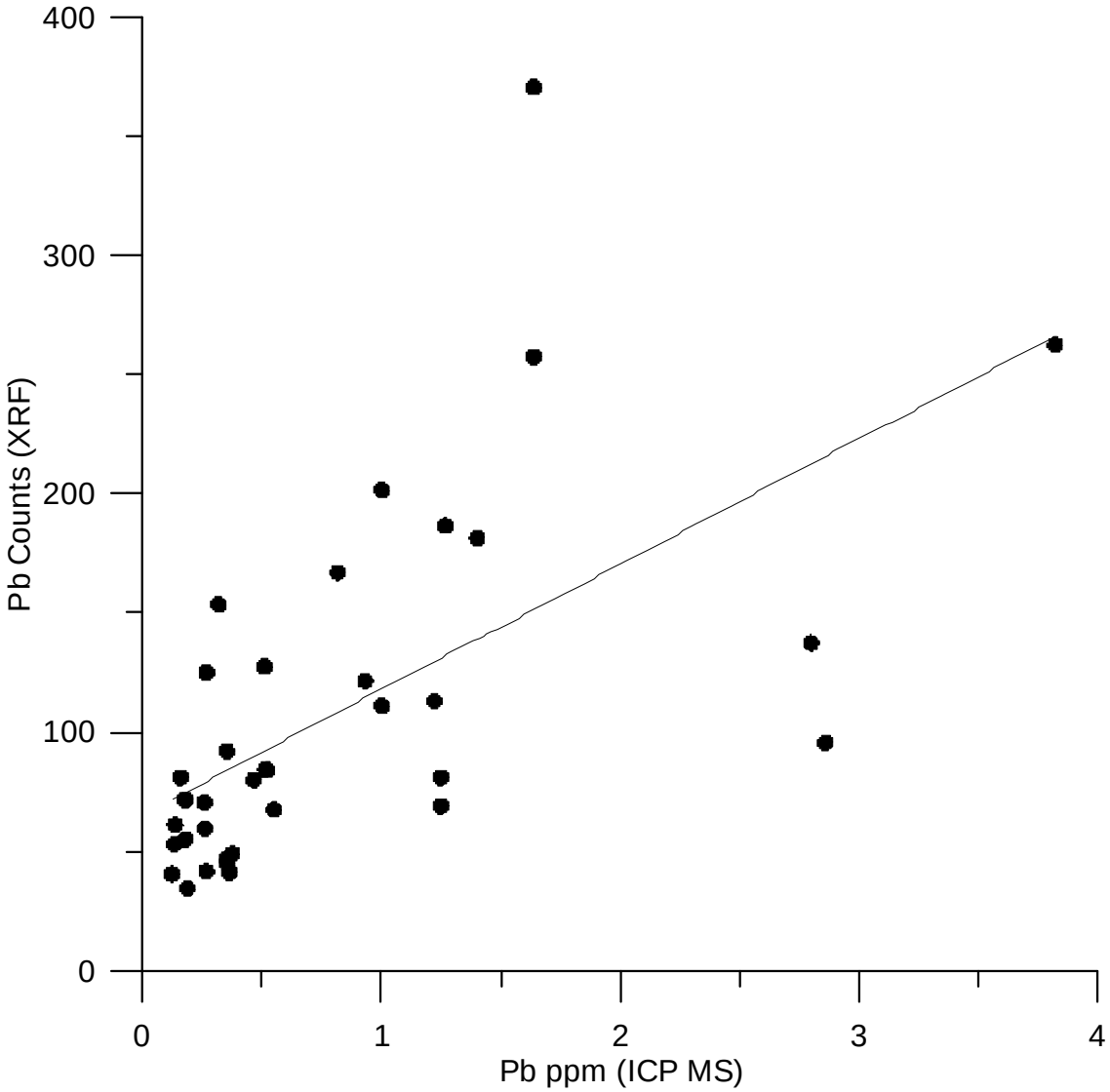

Figure S2-4: Comparison of concentration of Pb measured using ICPMS with the intensity derived from the XRF at a lag of 2 cm between working and archive halves of the core.

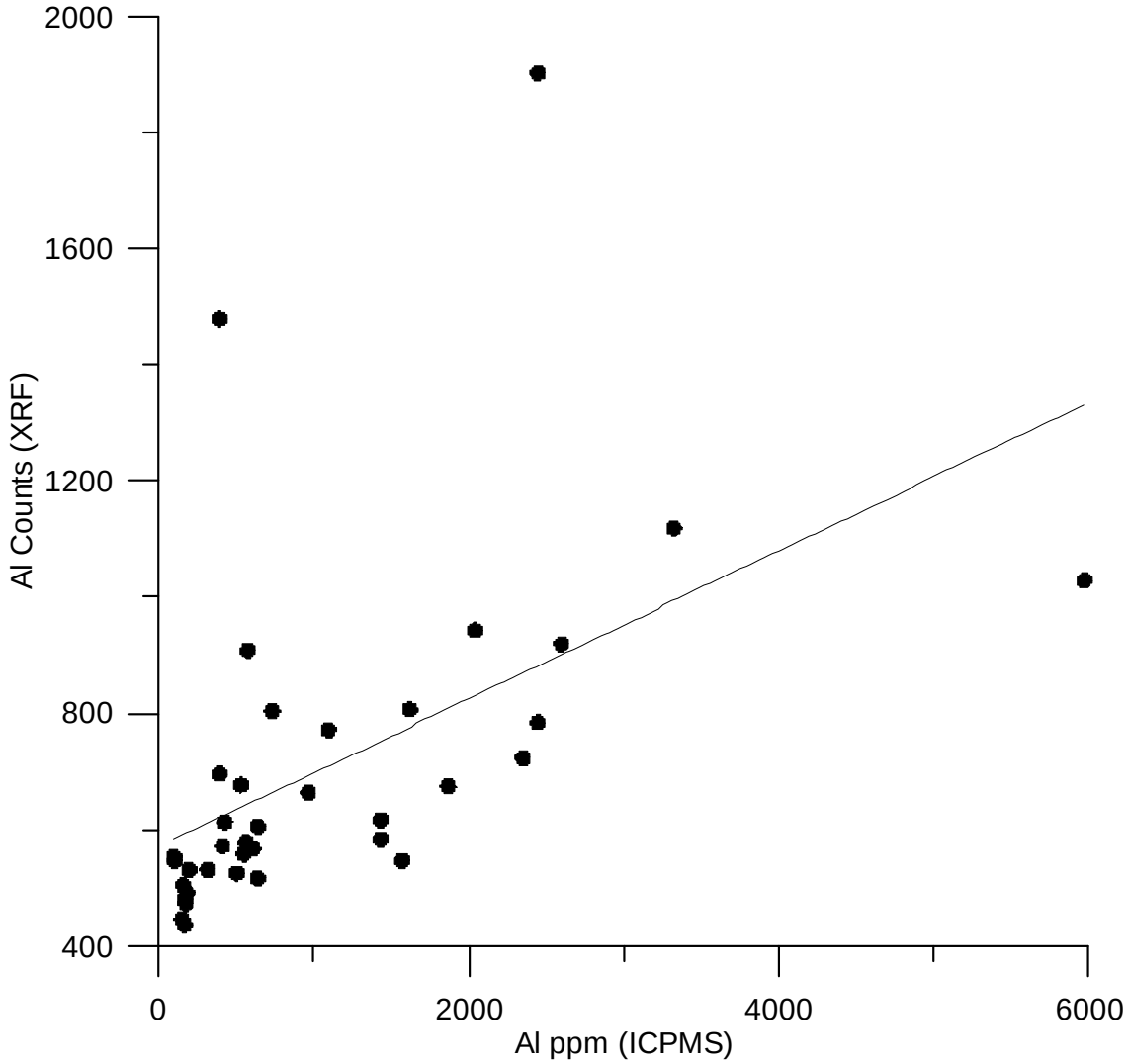

Figure S2-5: Comparison of concentration of Al measured using ICPMS with the intensity derived from the XRF at a lag of 2 cm between working and archive halves of the core.

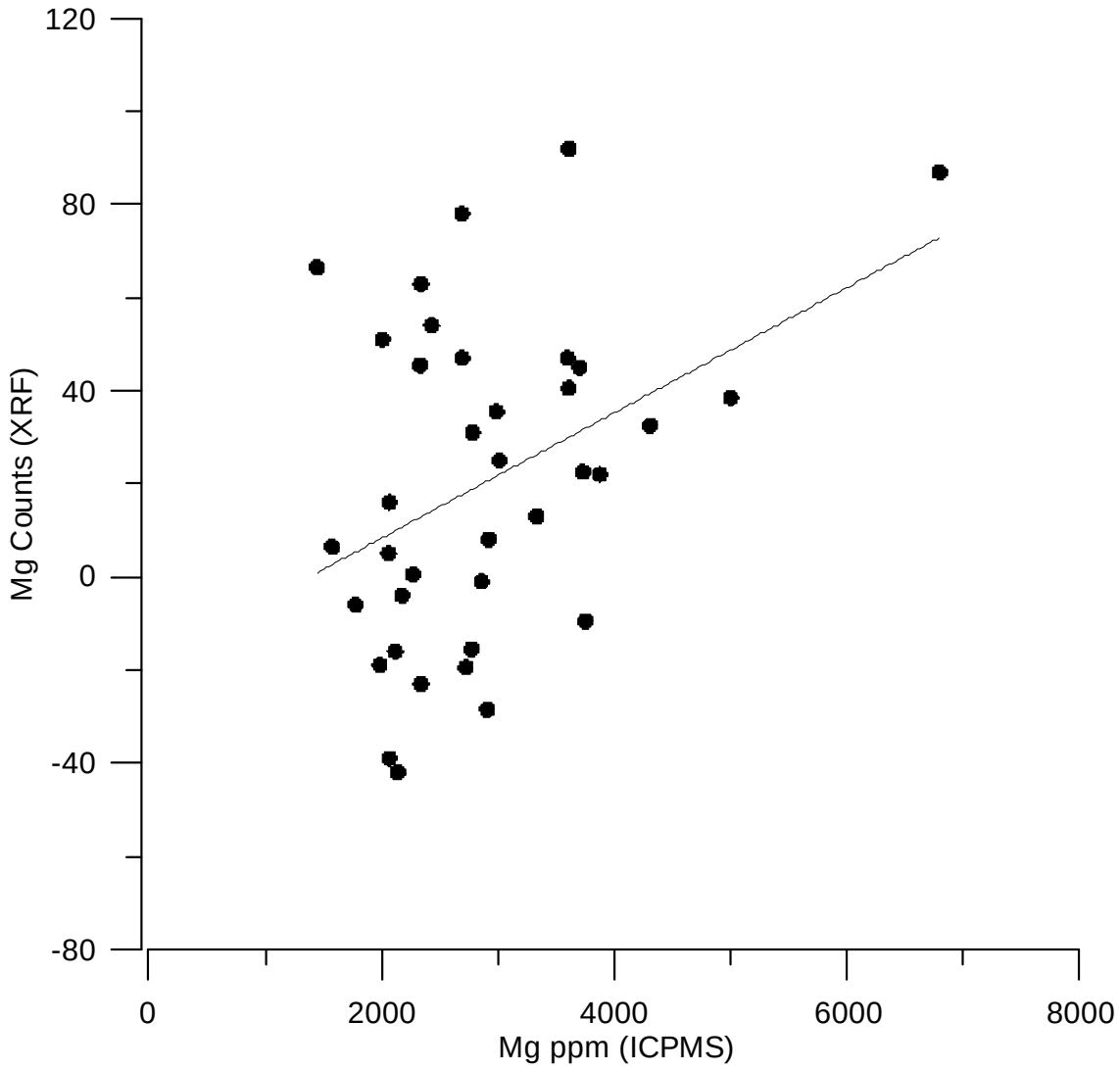

Figure S2-6: Comparison of concentration of Mg measured using ICPMS with the intensity derived from the XRF at a lag of 2 cm between working and archive halves of the core.

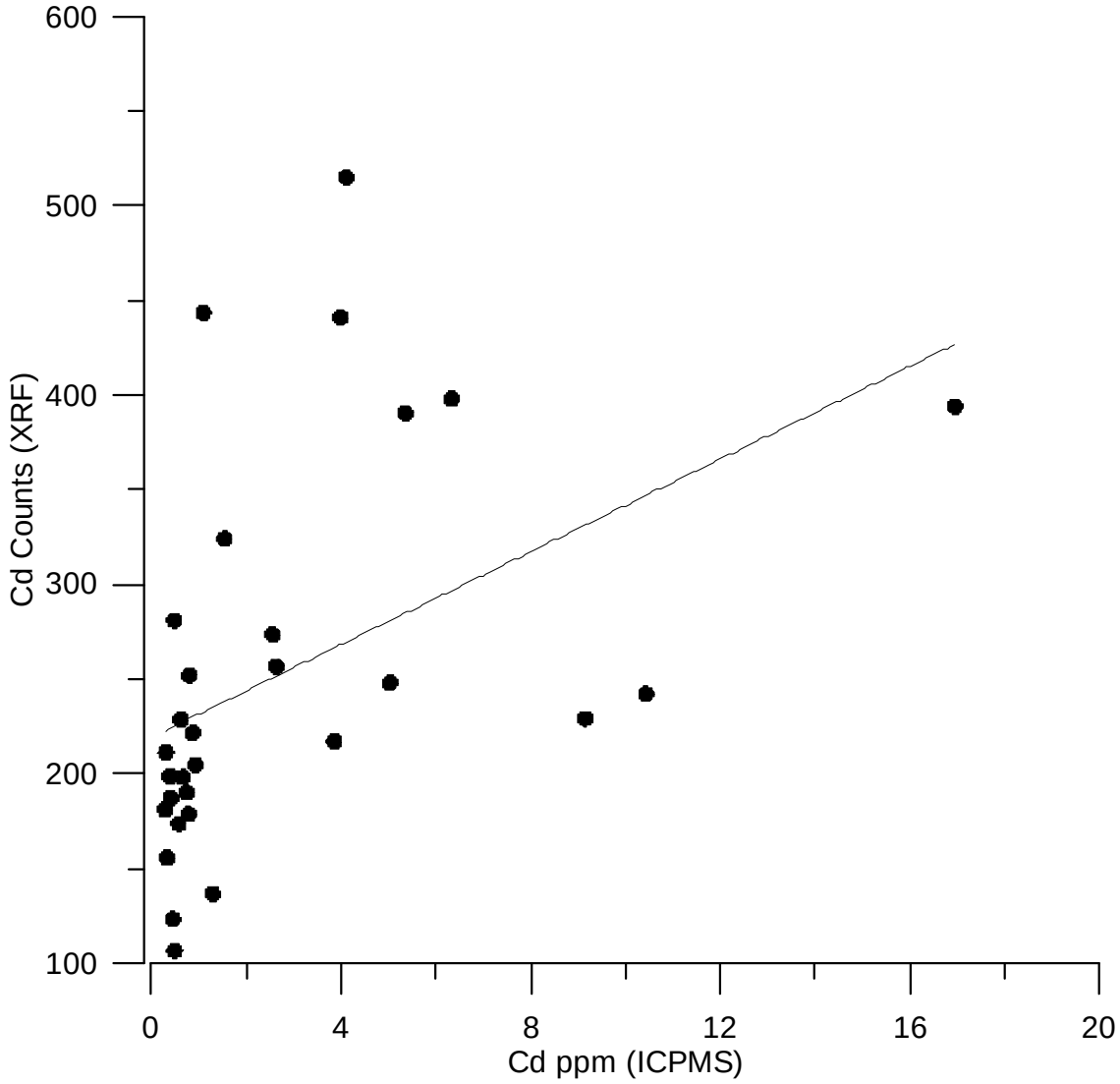

Figure S2-7: Comparison of concentration of Cd measured using ICPMS with the intensity derived from the XRF at a lag of 2 cm between working and archive halves of the core.

Comparison between Scanning XRF and Quantitative XRF

In order to evaluate the reliability of the analysis of certain elements (Fe, Al, Sr, Si K, Ca, Br, Mo, and Ba), a companion study (Kunkelova et al., 2018) analyzed samples of pressed pellets using a fully quantitative conventional XRF method. Here we report on the correlation between the R^2 values between the intensities and the concentrations are shown in Table S1-2. These show a range of between < 0.01 and >0.9. In most instances the low correlation coefficients arise as a result low concentration of the element (i.e. Mg, Pb, Cr, Ba, Zn, Ti, and Ni) leading to low sensitivity. In other instances (i.e. Ca) it could result of the relatively invariant concentration within the samples analyzed. The fact that some elements (Fe, Sr, Al, Si, K, and Br) all show high correlation coefficients provides confidence that variations in the intensity of the signal derived from the scanning XRF reflect true variations within the measured section.

Fe	0.79
Sr	0.77
Mo	0.01
Pb	
Cr	0.01
Ba	0.00
AL	0.84
Mg	0.12
Cd	
Si	0.89
K	0.90
Ca	0.02
Br	0.48
Zn	0.02
Ni	0.04
Ti	0.18

Table S1-2: Correlation between intensities made using the scanning XRF and the quantitative XRF on the identical samples. Samples highlighted in red are statistically significant ($p<0.05$).

Supplemental Material S3: Correlation between TOC and ICP-MS Data

The following section contains graphs of the correlation between the percentile of organic material and elements measuring using ICP-MS from Section U1466B-56R-1 between 789.65 and 790.8 mbsf.

Correlation coefficients between the concentration of organic carbon, organic nitrogen, CN ratio, $\delta^{13}C_{inoganic}$, $\delta^{18}O_{inorganic}$, $\delta^{13}C_{organic}$, $\delta^{13}N_{organic}$, and all the major and trace elements are included in Table S2-1.

Factor analysis of the data are shown in Figure S2-12 and Table S2-2.

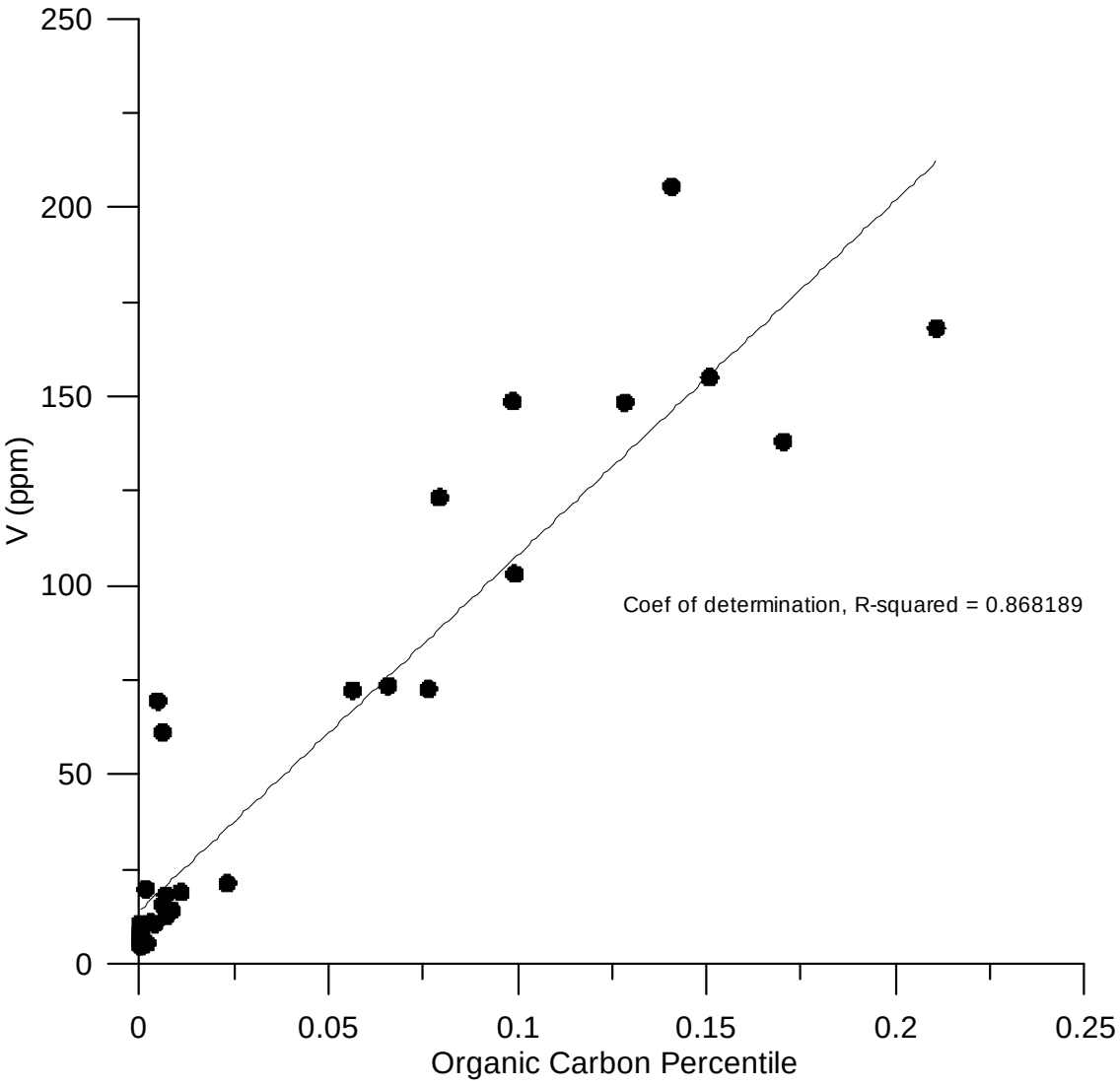

Figure S3-1: Correlation between the percentile organic carbon and concentration of V using ICP-MS.

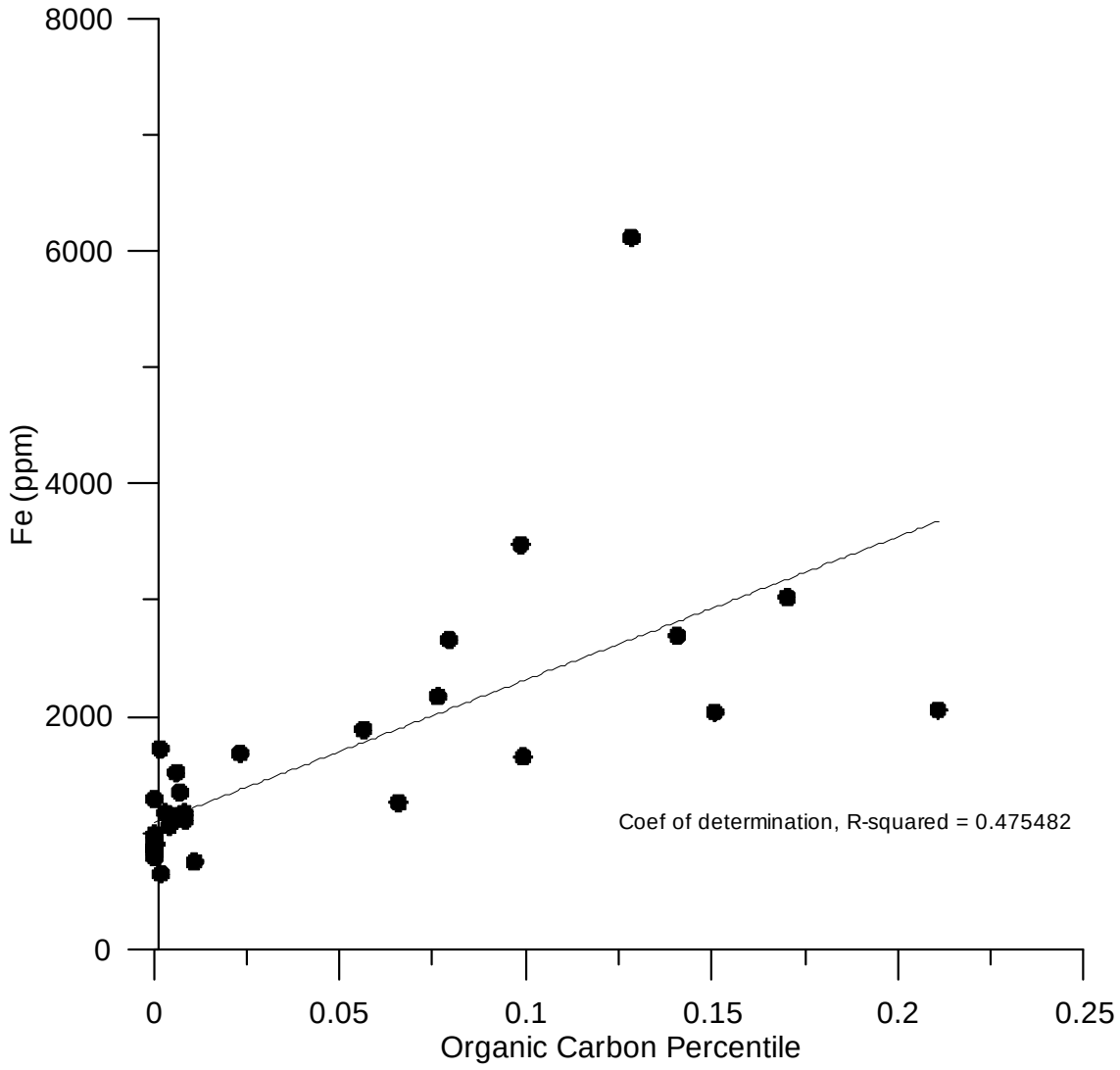

Figure S3-2: Correlation between the percentile organic carbon and concentration of Fe using ICP-MS.

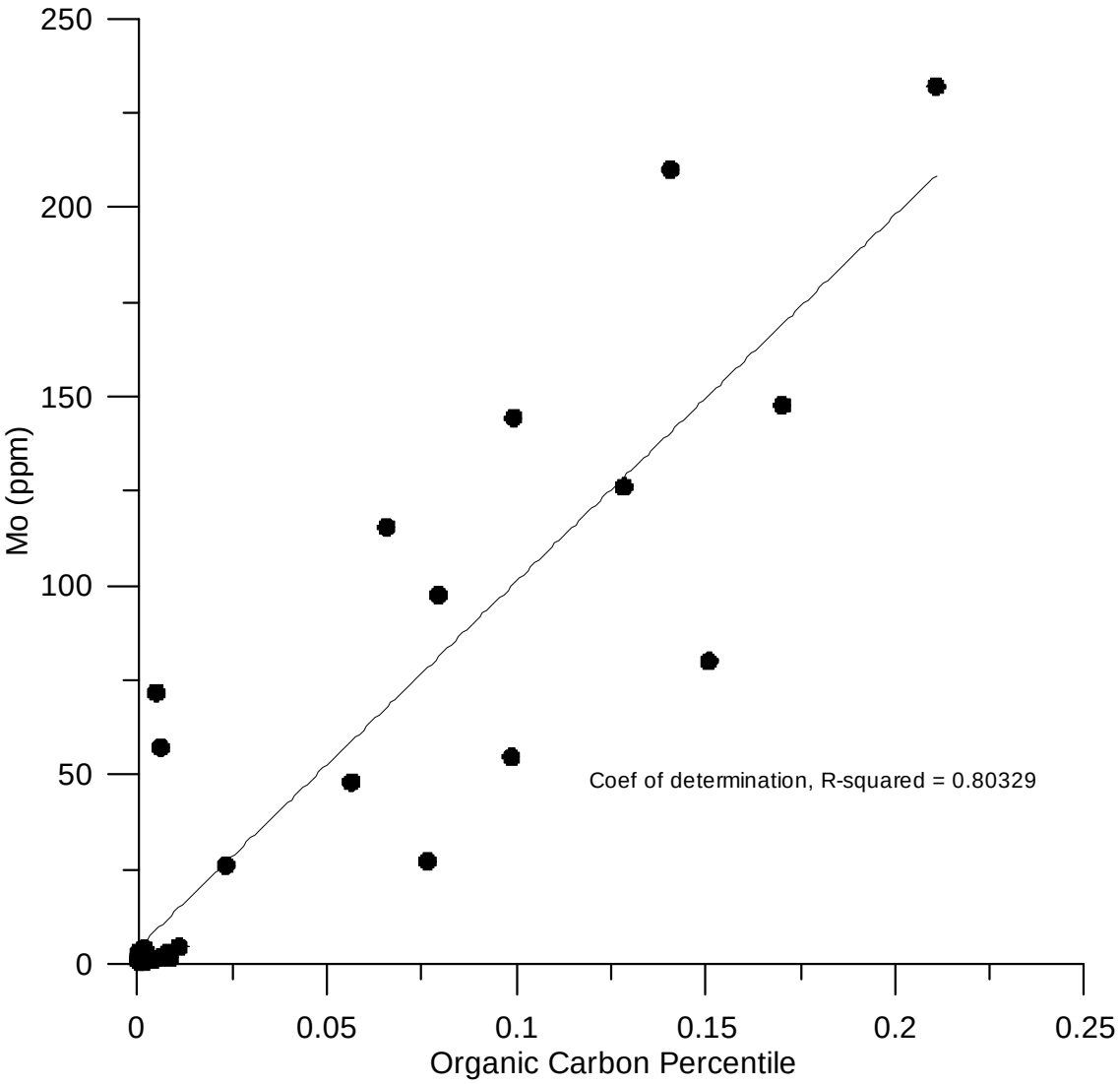

Figure S3-3: Correlation between the percentile organic carbon and concentration of Mo using ICP-MS.

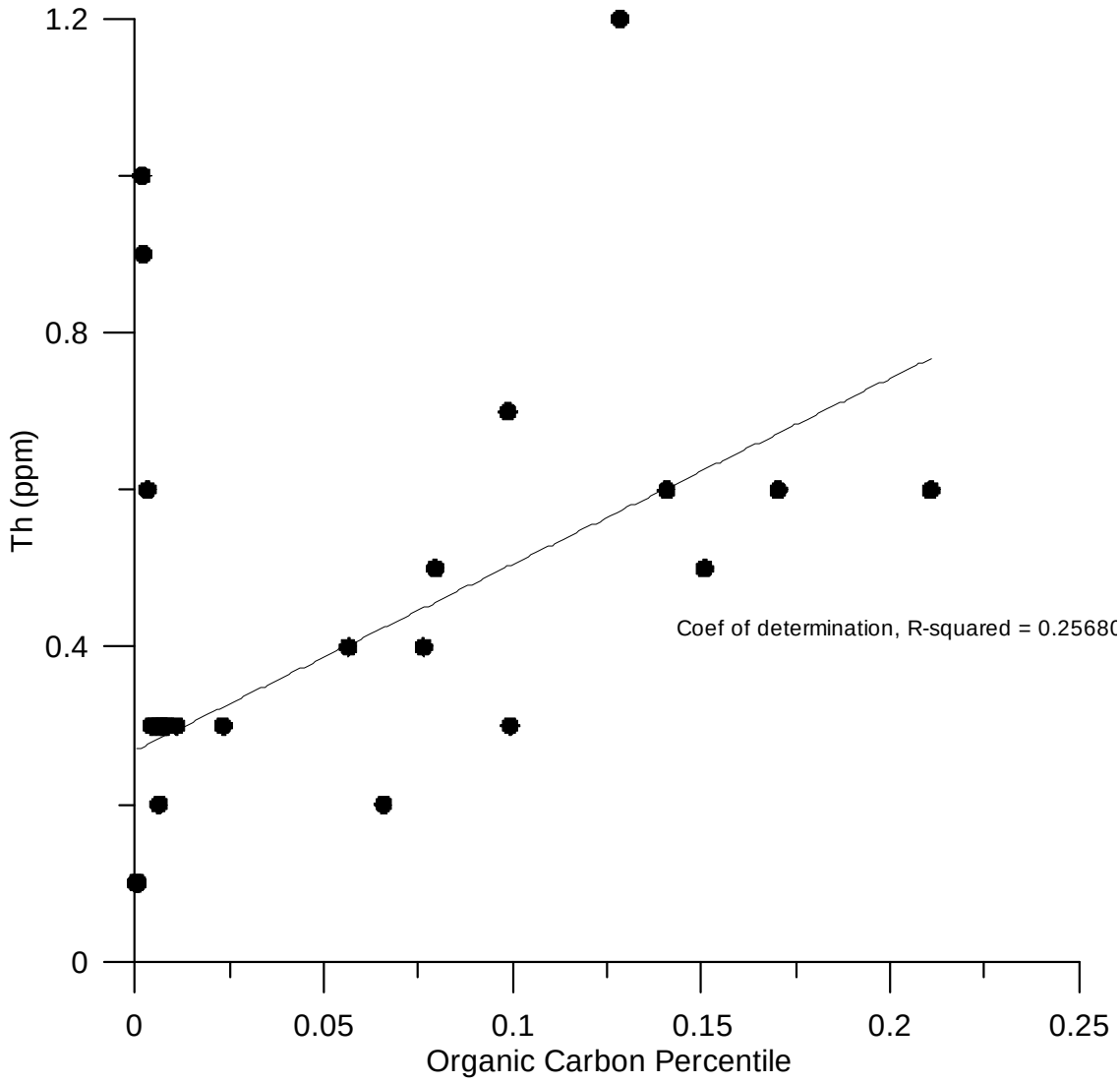

Figure S3-4: Correlation between the percentile organic carbon and concentration of Th using ICP-MS.

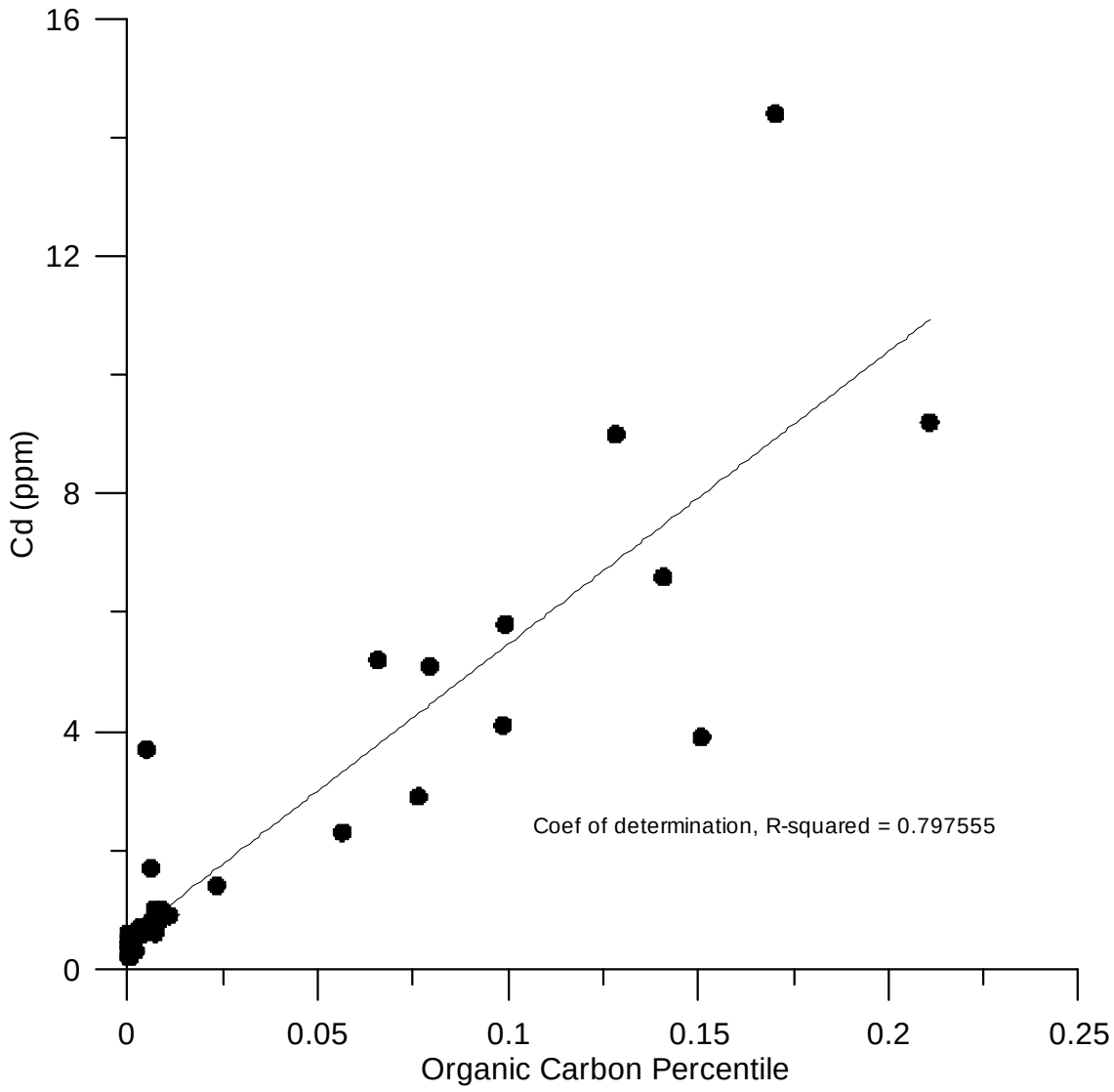

Figure S3-5: Correlation between the percentile organic carbon and concentration of Cd using ICP-MS.

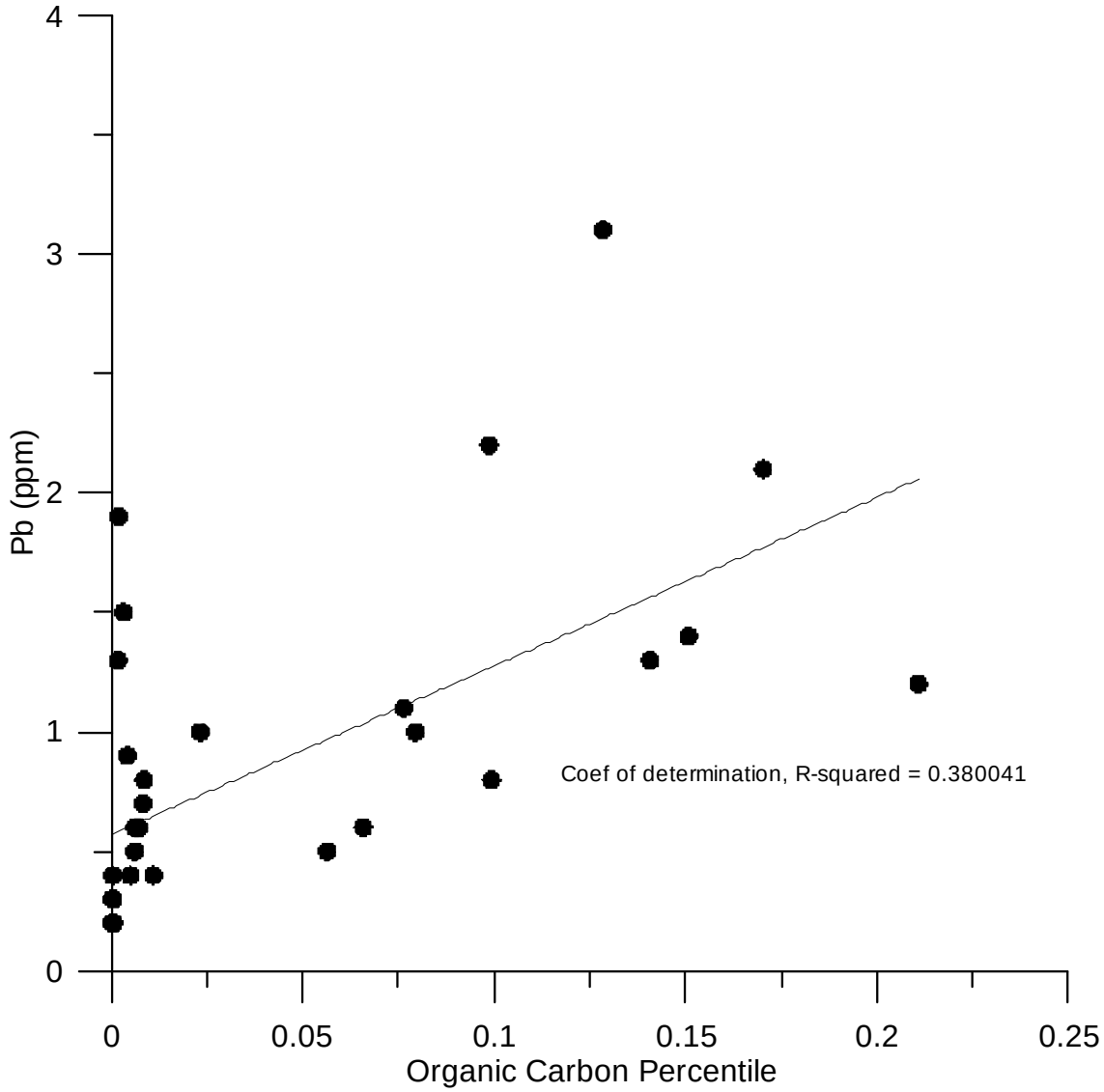

Figure S3-6: Correlation between the percentile organic carbon and concentration of Pb using ICP-MS.

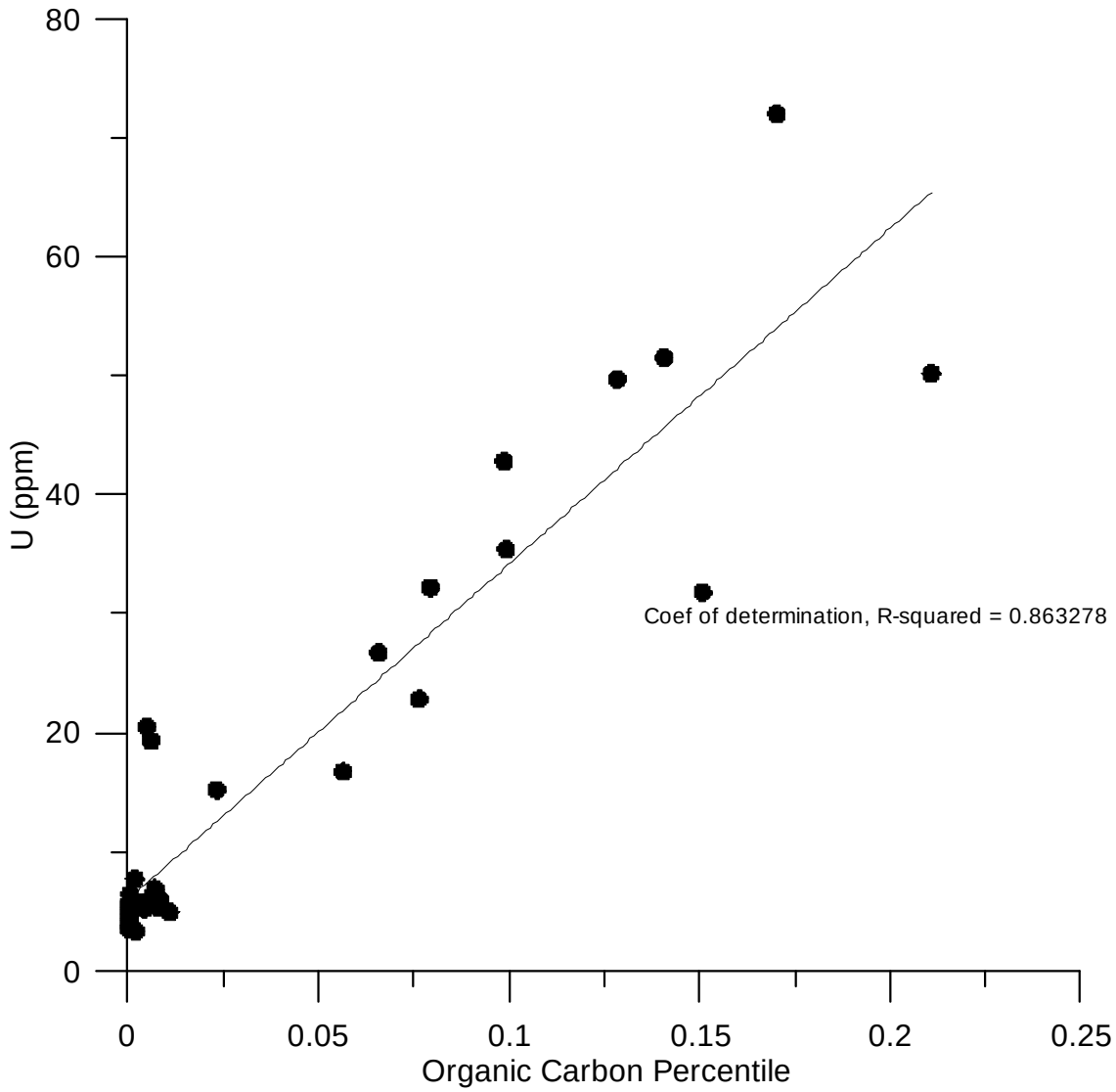

Figure S3-7: Correlation between the percentile organic carbon and concentration of U using ICP-MS.

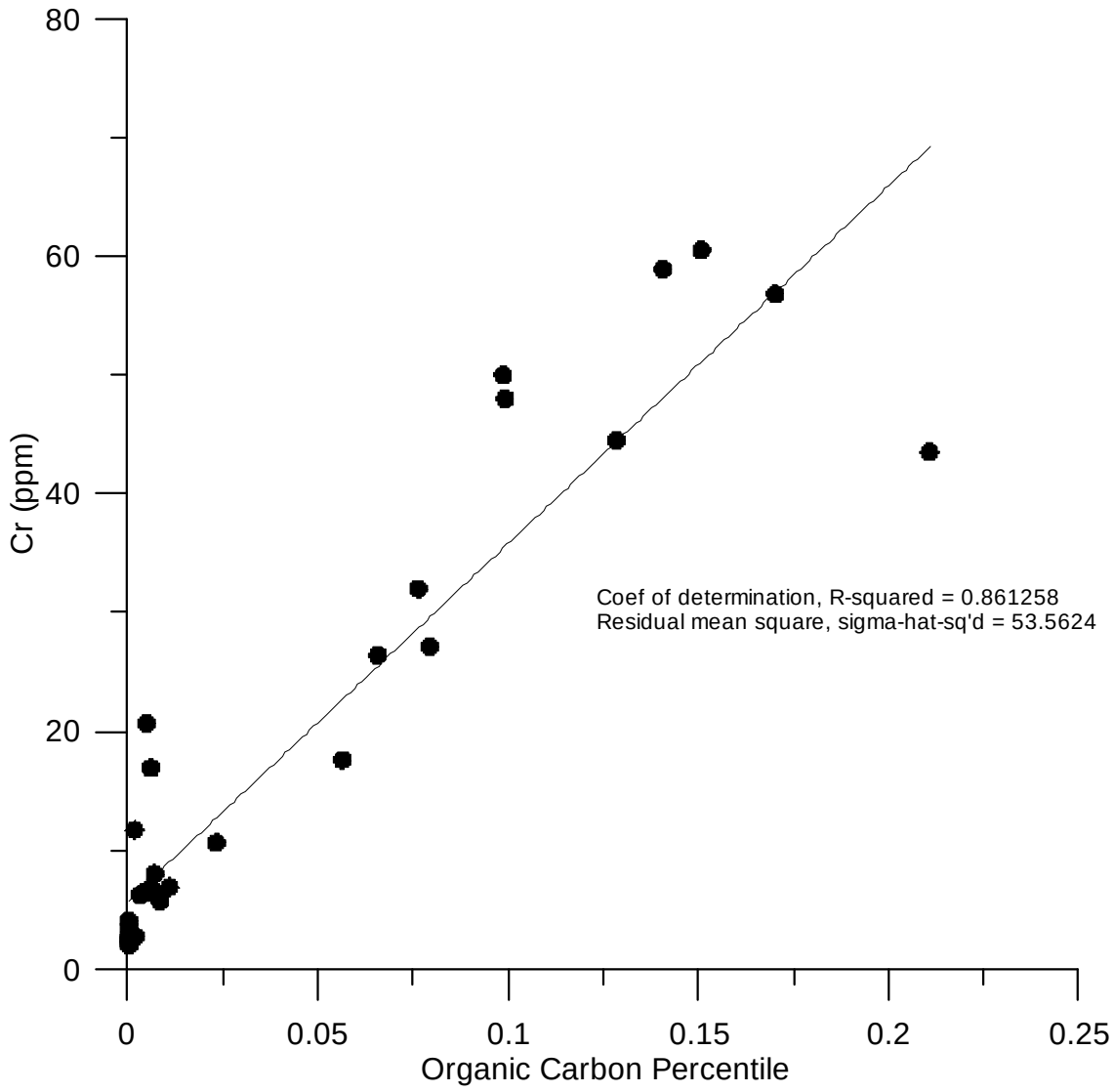

Figure S3-8: Correlation between the percentile organic carbon and concentration of Cr using ICP-MS.

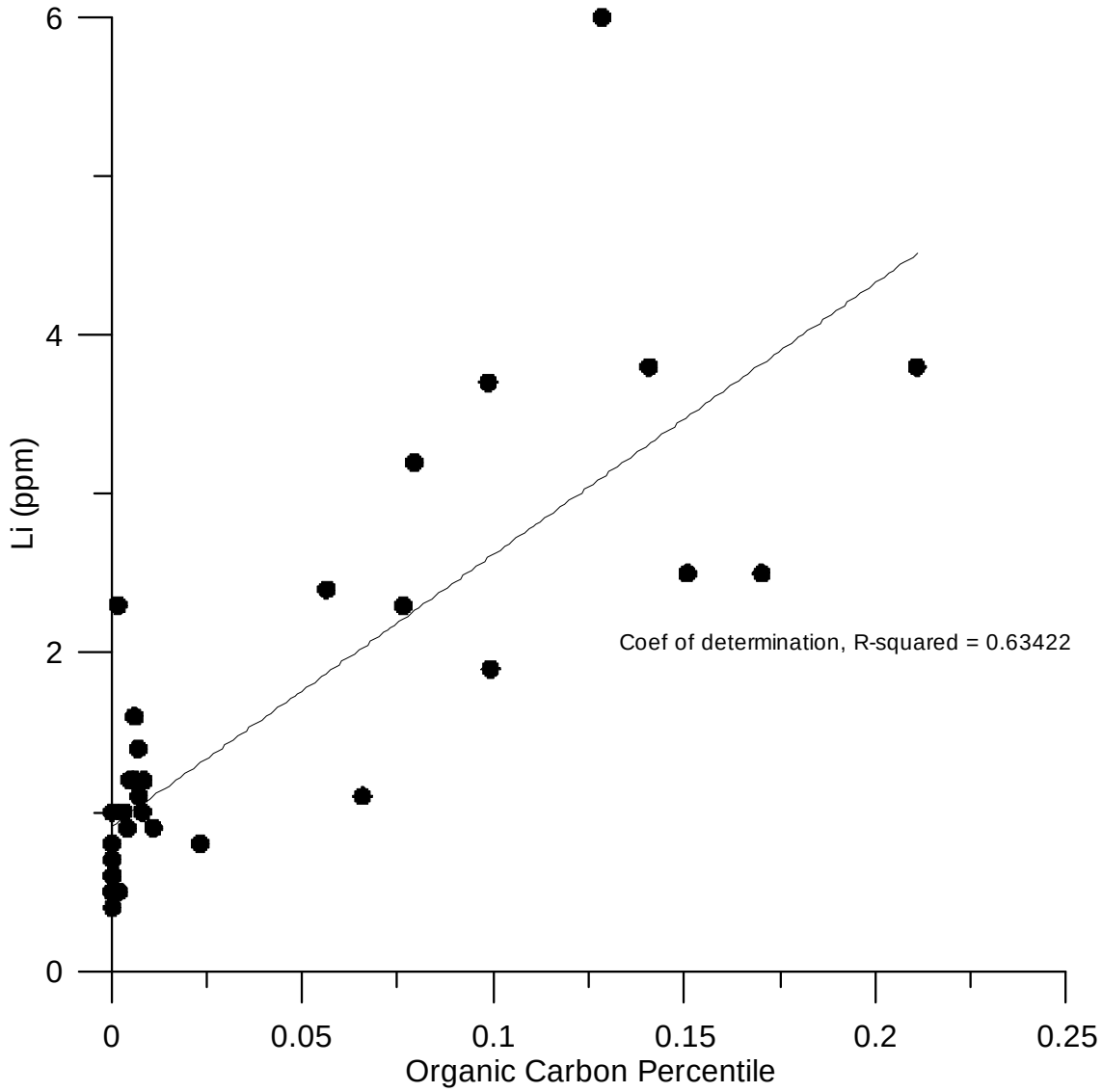

Figure S3-9: Correlation between the percentile organic carbon and concentration of Li using ICP-MS.

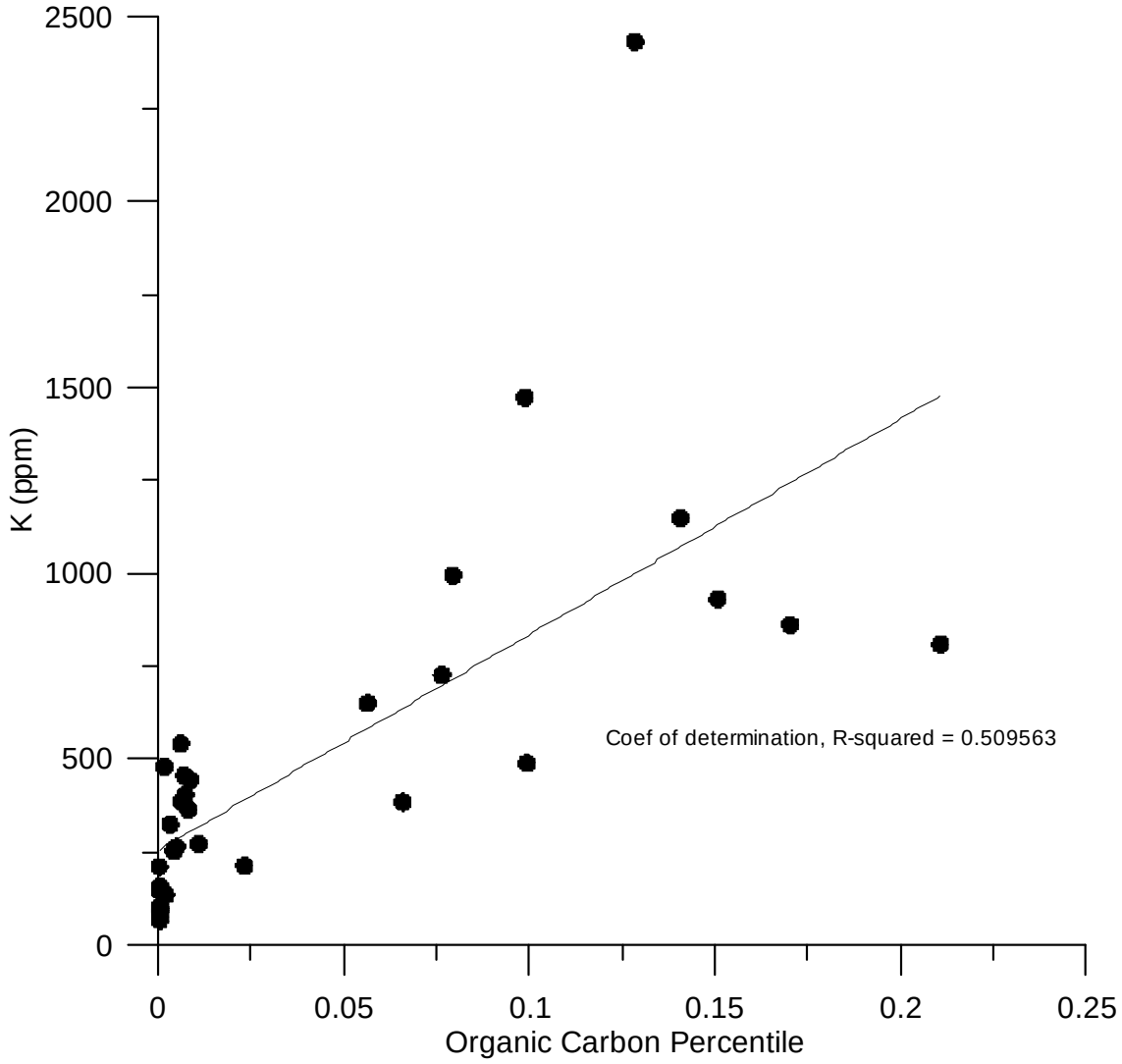

Figure S3-10: Correlation between the percentile organic carbon and concentration of K using ICP-MS.

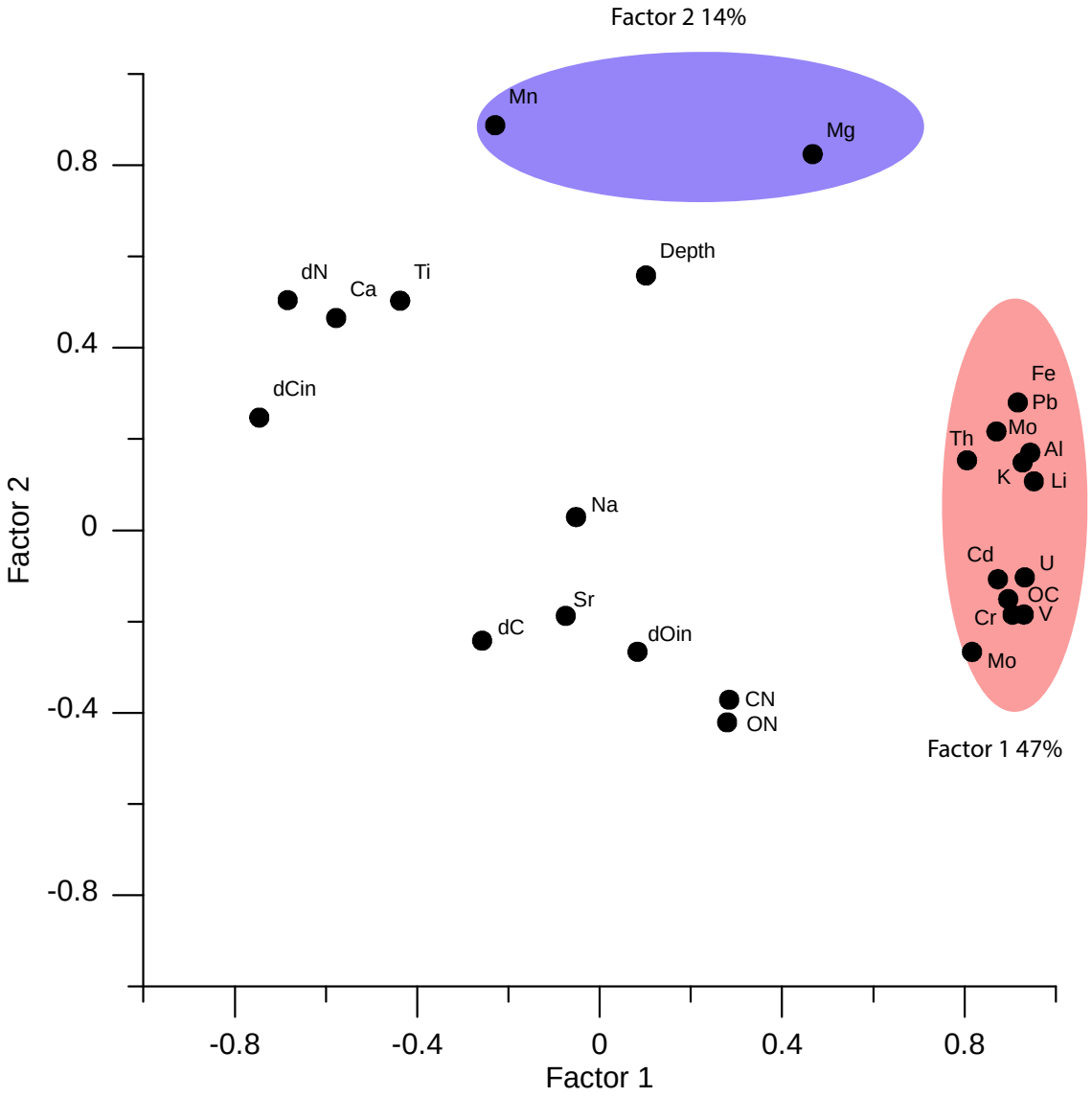

Figure S3-11: Principal component analysis of ICPMS data identifying three components which account for 73% of the variance. Above shows the correlation between Factor 1 and Factor 2. Data within the ovals show loading > 0.7.

	Means	Std.Dev.	Depth	d15N	d13C	N%	C%	CN	d13Cin	d18Oin	Li	Na	Mg	Al	K	Ca	Ti	V	Cr	Mn	Fe	Sr	Mo	Cd	Pb	Th
Depth	790.2	0.22																								
d15N	0.0	0.97	0.25																							
d13C	-20.3	0.42	-0.25	0.09	1.00																					
N%	0.0	0.00	-0.15	-0.43	-0.14																					
C%	0.0	0.06	0.08	-0.69	-0.10	0.22																				
CN	17.3	3.19	-0.66	-0.38	0.17	0.38	0.25																			
d13Cin	1.1	0.44	-0.15	0.67	-0.05	-0.22	-0.73	-0.14																		
d18Oin	-1.9	0.31	-0.07	-0.31	-0.16	0.14	0.05	0.01	-0.04																	
Li	1.6	1.28	0.06	-0.59	-0.26	0.20	0.79	0.28	-0.70	0.08																
Na	4608.9	1697.91	-0.30	-0.05	0.21	0.00	-0.07	0.10	0.03	-0.20	-0.01															
Mg	2942.4	993.60	0.51	0.04	-0.16	-0.26	0.35	-0.14	-0.20	-0.18	0.51	0.04														
Al	1013.5	1149.32	0.12	-0.55	-0.34	0.21	0.73	0.23	-0.64	0.09	0.97	-0.05	0.55													
K	499.1	488.41	0.06	-0.58	-0.31	0.23	0.71	0.27	-0.62	0.12	0.96	0.04	0.53	0.99												
Ca	336388.1	64849.11	-0.07	0.52	0.10	-0.21	-0.54	0.00	0.60	-0.12	-0.47	0.32	0.12	-0.50	-0.46											
Ti	294.0	70.61	-0.04	0.41	0.15	-0.21	-0.46	0.15	0.53	-0.04	-0.32	0.10	0.22	-0.35	-0.32	0.87										
V	53.3	60.50	0.03	-0.73	-0.04	0.22	0.93	0.30	-0.82	0.13	0.86	-0.05	0.33	0.80	0.79	-0.58	-0.46									
Cr	18.3	19.46	0.05	-0.69	-0.01	0.23	0.93	0.31	-0.78	0.03	0.79	-0.07	0.30	0.76	0.75	-0.57	-0.44	0.96								
Mn	44.8	25.31	0.55	0.55	-0.01	-0.48	-0.27	-0.45	0.29	-0.23	-0.16	-0.01	0.72	-0.13	-0.16	0.51	0.52	-0.32	-0.33							
Fe	1609.1	1067.44	0.22	-0.51	-0.40	0.24	0.68	0.19	-0.56	0.08	0.93	-0.04	0.63	0.98	0.97	-0.42	-0.26	0.74	0.71	-0.02						
Sr	1677.3	363.81	-0.61	-0.14	-0.03	0.35	-0.11	0.59	0.22	0.10	0.02	0.41	-0.28	-0.05	0.02	0.52	0.47	-0.08	-0.08	-0.35	-0.06					
Mo	44.6	65.04	0.02	-0.70	0.00	0.21	0.89	0.27	-0.71	0.14	0.72	-0.05	0.22	0.63	0.60	-0.55	-0.46	0.90	0.85	-0.30	0.58	-0.09				
Cd	2.6	3.32	0.11	-0.65	-0.23	0.19	0.89	0.24	-0.63	0.06	0.73	-0.10	0.36	0.71	0.67	-0.59	-0.48	0.84	0.84	-0.21	0.71	-0.19	0.88			
Pb	0.8	0.67	0.06	-0.44	-0.36	0.31	0.68	0.28	-0.44	-0.04	0.84	-0.01	0.52	0.89	0.88	-0.38	-0.24	0.68	0.72	-0.11	0.90	0.04	0.51	0.69		
Th	0.3	0.27	-0.01	-0.32	-0.35	0.25	0.58	0.24	-0.44	-0.03	0.86	-0.05	0.37	0.87	0.83	-0.41	-0.28	0.63	0.62	-0.18	0.82	0.08	0.49	0.58	0.90	
U	17.8	18.20	0.16	-0.69	-0.18	0.24	0.93	0.25	-0.73	0.09	0.80	-0.09	0.38	0.78	0.75	-0.59	-0.46	0.93	0.93	-0.24	0.77	-0.16	0.90	0.96	0.74	0.62

Table S3-1: Correlation matrix of ICPMS, percent C and N, and isotopic data. Values in red show significant correlation at the 95% confidence limits.

	Factor - 1	Factor - 2	Factor - 3
Depth	-0.07333	0.804629	-0.279774
dN	0.72641	0.438625	0.103196
dC	0.23302	-0.242078	-0.113724
ON	-0.30728	-0.491290	0.077453
OC	-0.91027	-0.018920	-0.089858
CN	-0.28911	-0.640059	0.445096
dCin	0.77712	0.046759	0.266529
dOin	-0.10928	-0.223983	-0.125105
Li	-0.93069	0.102555	0.231112
Na	0.07538	-0.208578	0.421388
Mg	-0.38372	0.773377	0.393540
Al	-0.91814	0.176567	0.224815
K	-0.90013	0.118432	0.281959
Ca	0.64484	0.103922	0.643812
Ti	0.50959	0.141620	0.681751
V	-0.94580	-0.068646	-0.062370
Cr	-0.92109	-0.067770	-0.069652
Mn	0.30877	0.842163	0.256335
Fe	-0.87952	0.264845	0.285345
Sr	0.09616	-0.618233	0.707159
Mo	-0.84380	-0.115370	-0.169176
Cd	-0.88552	0.042328	-0.115011
Pb	-0.83442	0.150592	0.350650
Th	-0.77644	0.093357	0.311428
U	-0.94297	0.038720	-0.088403
Expl.Var	11.86319	3.549261	2.721456
Prp.Totl	0.47453	0.141970	0.108858

Table S3-2: Factor loadings of the geochemical parameters. Factors >0.7 are marked.

Supplemental S-4: Comparison with benthic oxygen isotope data

Comparison of record of benthic $\delta^{18}O$ values with data from U1466 and U1468.

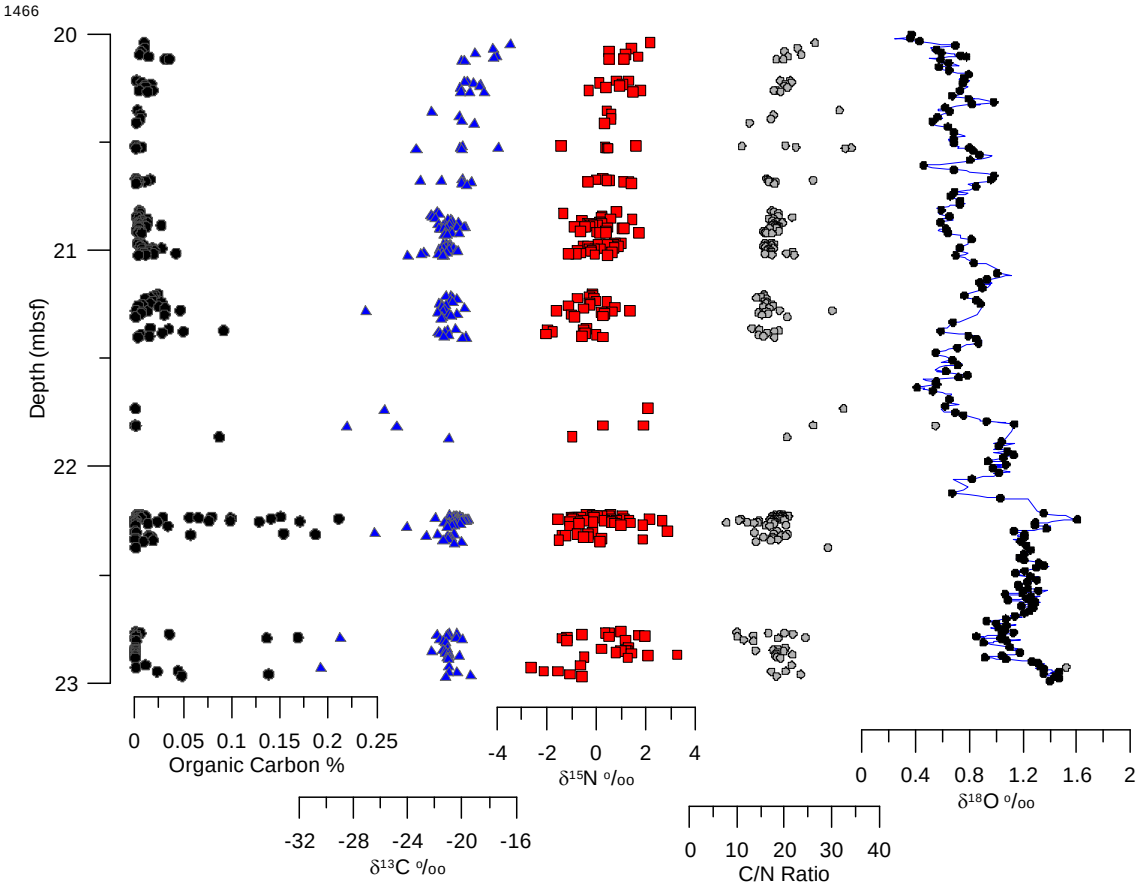

Figure S4-1: Reproduction of Figure 5 with $\delta^{18}O$ values from Zachos et al (2001). The d18O values show a gradual increase consistent with an increase in sea level during this period.

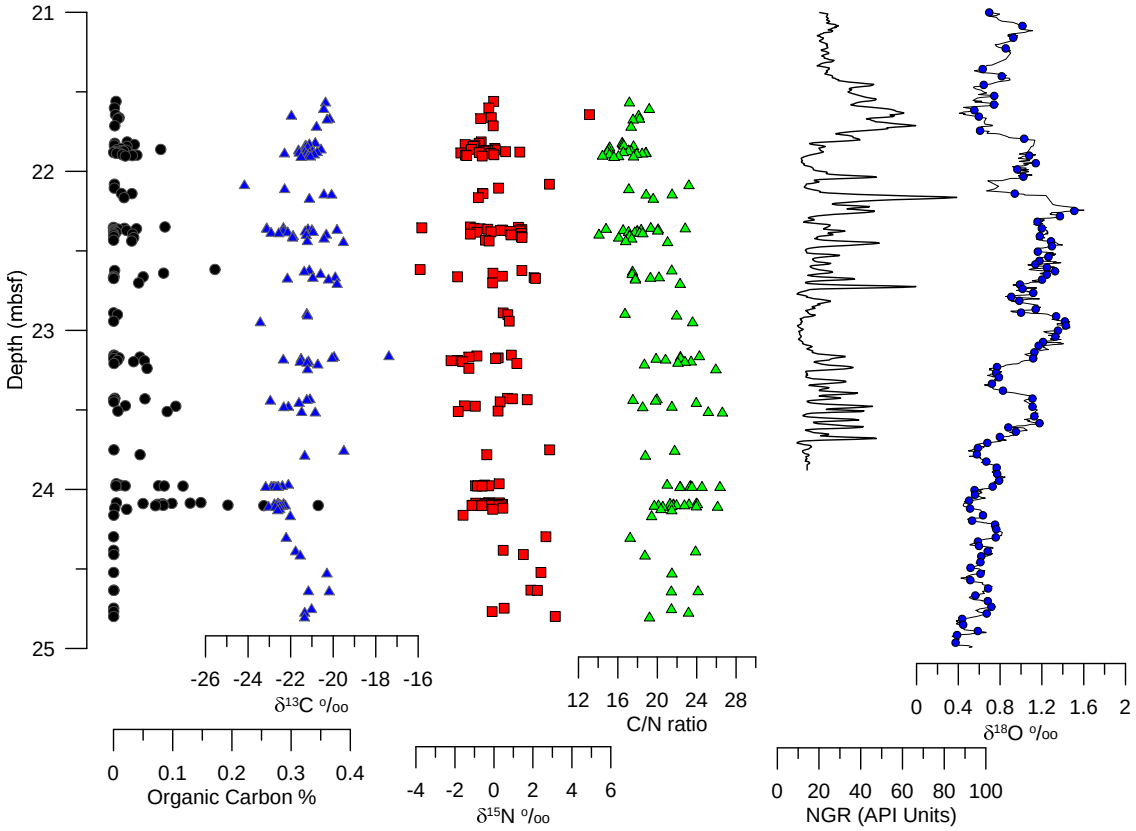

Figure S4-2: Reproduction of Figure 6 with $\delta^{18}O$ values from Zachos et al (2001).